On the deceleration of Fanaroff–Riley Class I jets: mass loading of magnetized jets by stellar winds

Andreu Anglés-Castillo,[1,2] Manel Perucho [ORCID],[1,3]* José María Martí[1,3] and Robert A. Laing[4]

[1]*Departament d'Astronomia i Astrofísica, Universitat de València, C/ Dr. Moliner, 50, E-46100 Burjassot, València, Spain*
[2]*Departament de Física Teòrica & IFIC, Universitat de València-CSIC, C/ Dr. Moliner, 50, E-46100 Burjassot, València, Spain*
[3]*Observatori Astronòmic, Universitat de València, C/ Catedràtic José Beltrán 2, E-46980 Paterna, València, Spain*
[4]*Square Kilometre Array Organisation, Jodrell Bank Observatory, Lower Withington, Macclesfield, Cheshire SK11 9FT, UK*

ABSTRACT

In this paper, we present steady-state relativistic magnetohydrodynamic simulations that include a mass-load term to study the process of jet deceleration. The mass load mimics the injection of a proton–electron plasma from stellar winds within the host galaxy into initially pair plasma jets, with mean stellar mass-losses ranging from 10^{-14} to 10^{-9} $M_\odot$ yr^{-1}. The spatial jet evolution covers ~ 500 pc from jet injection in the grid at 10 pc from the jet nozzle. Our simulations use a relativistic gas equation of state and a pressure profile for the ambient medium. We compare these simulations with previous dynamical simulations of relativistic, non-magnetized jets. Our results show that toroidal magnetic fields can prevent fast jet expansion and the subsequent embedding of further stars via magnetic tension. In this sense, magnetic fields avoid a runaway deceleration process. Furthermore, when the mass load is large enough to increase the jet density and produce fast, differential jet expansion, the conversion of magnetic energy flux into kinetic energy flux (i.e. magnetic acceleration), helps to delay the deceleration process with respect to non-magnetized jets. We conclude that the typical stellar population in elliptical galaxies cannot explain jet deceleration in classical Fanaroff–Riley type I radio galaxies. However, we observe a significant change in the jet composition, thermodynamical parameters, and energy dissipation along its evolution, even for moderate values of the mass load.

Key words: relativistic processes – stars: winds, outflows – galaxies: active – galaxies: jets.

1 INTRODUCTION

Jets from radio-loud active galactic nuclei (AGNs) are separated into two main classes, namely FR I and FR II (Fanaroff–Riley type), following their large-scale morphology and radio luminosity (Fanaroff & Riley 1974). FR I jets are decollimated at kiloparsec scales and show diffuse emission at their edges (e.g. 3C 31; Laing & Bridle 2002a). On the contrary, the more powerful FR II jets remain highly collimated and supersonic until the reverse shock (hotspots, e.g. Cyg A; Carilli & Barthel 1996). Despite their different morphology at large scales both types of sources show relativistic speeds at parsec scales, with differences associated with the transversal structure of the axial velocity and with a trend towards smaller velocities in the case of FR I jets (Giovannini et al. 2001; Celotti & Ghisellini 2008; Meyer et al. 2011).

The deceleration of these jets is deduced by the symmetrization of the jet and counter-jet brightness, which implies non-relativistic flow velocity at kiloparsec scales (Laing & Bridle 2014, and references therein). The most widely accepted explanation of FR I jet deceleration at kpc scales relates it to entrainment of colder and denser ambient gas (Bicknell 1984; Laing 1993, 1996) via a mixing shear layer (De Young 1986, 1993; Bicknell 1994; Wang et al. 2009). The growth of Kelvin–Helmholtz instability pinching modes after a

strong recollimation shock (Perucho & Martí 2007) has also been proposed as a destabilizing mechanism. Rossi et al. (2008) discussed the deceleration of FR I jets by the growth of helical instabilities in a jet propagating through a homogeneous ambient medium. From an observational point of view, Worrall et al. (2007) studied the possible relation between the X-ray helical structure observed in the powerful FR I jet ($\sim 10^{44}$ erg s^{-1}) in NGC 315 and the development of instabilities, but no clear conclusions could be derived.

A recent paper (Gourgouliatos & Komissarov 2018a) proposes the development of the relativistic centrifugal instability (Gourgouliatos & Komissarov 2018b), after the generation of a conical recollimation shock at hundreds of parsecs from the jet source. The recollimation shock is produced due to jet overpressure when propagating through a galactic atmosphere with decreasing pressure. The development of the centrifugal instability would imply entrainment by small-scale eddies growing at the jet boundary and propagating towards the jet axis with time/distance.

A second option, which might be complementary to turbulent entrainment from the jet boundary, is mass load by stellar mass-loss (Phinney 1983; Komissarov 1994; Bowman, Leahy & Komissarov 1996; Laing & Bridle 2002b; Hubbard & Blackman 2006). Komissarov (1994) showed that the interaction between the jet flow and the stellar winds from stars that may go through the jet cross-section as they orbit in the potential of the galaxy, can be treated as a hydrodynamical problem. The reason is that the gyroradii of the particles are much smaller than the size of the interaction region

* E-mail: manel.perucho@uv.es

between the jet and the stellar wind. Thus, this situation can be modelled as a distributed source of mass injected into the jet. The first work dealing with this scenario was published by Bowman et al. (1996). In that paper, the authors studied the steady-state structure of jets subject to mass load. They focused on low power, light and hot (non-magnetized) electron/proton jets, and concluded that the simulated jets could be efficiently decelerated by a population of old, low-mass stars within the typical FR I deceleration distance. A difference was noted between hotter and colder jets, because the former tend to cool down due to the entrainment of the colder wind particles, whereas the latter showed an increase in temperature due to the dissipation of kinetic energy associated with deceleration.

Hubbard & Blackman (2006) performed an analytical study of the parameter space for stellar mass-loss rates from massive stars and jet powers that could end up in efficient jet deceleration. The authors derived the following useful relation by considering the deceleration distance as the distance at which the kinetic energy required to accelerate the loaded mass is approximately equal to the total initial jet kinetic power. The resulting expression, as given in Perucho et al. (2014), is

$$l_d \simeq \frac{1}{\gamma_j} \left(\frac{L_j}{10^{43} \mathrm{erg\,s^{-1}}} \right) \left(\frac{\dot{M}}{10^{-11} \mathrm{M_\odot yr^{-1}}} \right)^{-1}$$
$$\times \left(\frac{n_s}{\mathrm{pc^{-3}}} \right)^{-1} \left(\frac{R_j}{10 \mathrm{pc}} \right)^{-2} 10^2 \mathrm{\,kpc}, \qquad (1)$$

where γ_j is the jet Lorentz factor, L_j is its kinetic power, R_j is the jet radius, $\dot{M}$ is the mean mass-loss rate of the stellar population in the galaxy, and n_s is the number of stars per unit volume. This last parameter is obviously a decreasing function of distance to the galactic nucleus, so the expression stands as a lower limit to the deceleration distance.

A number of works by Laing & Bridle (e.g. Laing & Bridle 2002a, b, 2014) have characterized the jet deceleration region as a typically extended region in which kinetic energy seems to be dissipated and the jet becomes X-ray bright (Laing & Bridle 2014). The authors conclude that entrainment is a gradual process that extends from the boundaries to the axis: the already slower outer layers of jets (e.g. M87, CenA, NGC 1052; Müller et al. 2014; Baczko et al. 2016; Walker et al. 2018) could be decelerated on shorter scales than the faster spines. Furthermore, they also point out that stellar mass load can be more efficient in low-power FR I jets (e.g. M84 and NGC 193). In these sources, no obvious transverse velocity gradients were found, which is more consistent with distributed mass load than with entrainment from the jet boundaries. Wykes et al. (2013, 2015) have discussed the dynamical role of stellar mass load in the jet in Centaurus A, in the context of kinetic energy dissipation and particle acceleration, considering a detailed modellization of the stellar population in the galaxy that includes a mixture of old and young stars. These works conclude that a large number of stars ($\sim 10^8$) could be located inside the jet, efficiently contributing to jet dynamics and non-thermal emission. On the contrary, in Laing & Bridle (2002a, b), the authors used a one-dimensional model of the source properties that required growing entrainment with distance to explain the jet and counter-jet properties in the more powerful (10^{44} erg s^{-1}) FR I jet 3C 31. They concluded that mass entrainment by stellar winds could not be the main decelerating mechanism because the star number density is expected to fall with distance to the Galactic Centre, so the entrainment mechanism was more likely to be ambient gas mixing through the jet shear layer.

Perucho et al. (2014) presented a number of dynamic simulations based on the parameter space used by Bowman et al. (1996). The

simulations showed that low-power jets ($L_j \leq 10^{42}$ erg s^{-1}) can be efficiently decelerated by a population of old, low-mass stars. The entrainment develops a runaway deceleration effect by increasing the jet thermal pressure, which triggers expansion and therefore an increased mass load by the newly embedded stars. The jet expansion and deceleration causes a drop of the momentum flux per unit area, which brings the jet head close to stagnation. Nevertheless, there is a threshold of jet power, at a given mean stellar mass-loss rate, that can be estimated using equation (1), over which stellar mass load has a marginal or negligible effect on the jet.

A recent paper (Perucho 2020) suggests that in the case of FR I jets with $L_j \sim 10^{43}$ erg s^{-1}, the interaction of stars with the jet boundary as they enter or leave the jet could act as a trigger for turbulent mixing between the jet flow and the surrounding interstellar medium at tens to hundreds of parsecs (see also Torres-Albà 2020). The author proposed this solution for the triggering mechanism of FR I jet deceleration, based on the agreement of the time and spatial scales of this process with the observed deceleration scales (Laing & Bridle 2014).

Different studies have reported that the interaction between jets and stars can lead to efficient energy dissipation and high-energy emission (e.g. Bednarek & Protheroe 1997; Barkov, Aharonian & Bosch-Ramon 2010; Barkov et al. 2012; Bosch-Ramon, Perucho & Barkov 2012; Araudo, Bosch-Ramon & Romero 2013; Wykes et al. 2013, 2015; Aharonian, Barkov & Khangulyan 2017; Perucho, Bosch-Ramon & Barkov 2017; Vieyro, Torres-Albà & Bosch-Ramon 2017; Torres-Albà & Bosch-Ramon 2019). Furthermore, the injection of protons in pair jets and the strong shocks generated have been suggested to be (and studied as) a possible source of proton acceleration and neutrino production (e.g. Bosch-Ramon et al. 2012; Murase, Oikonomou & Petropoulou 2018).

In this paper, we present an extension of Perucho et al. (2014) to magnetized jets with a jet power of 10^{43} erg s^{-1}. The simulations presented here generate the steady-state structure of the mass-loaded jets following the approach of Komissarov, Porth & Lyutikov (2015; see also Fuentes et al. 2018), in order to study the structure of steady, narrow, axisymmetric relativistic flows using one-dimensional time-dependent simulations. This simplification has allowed us to run a large number of models, spanning several orders of magnitude in rest-mass density and internal energy, and three different values of the Lorentz factor. The stellar winds are included in the calculations as a source term in mass, in the same way as was done in Perucho et al. (2014). It is important to stress that our paper focuses on one of the two main strategies that have been followed to study this scenario, i.e. we study the possible global effect of mass load by a distribution of stars along the jet flow channel, unlike other works that have focused on single jet–star interactions (e.g. Hubbard & Blackman 2006; Bosch-Ramon et al. 2012; Perucho et al. 2017).

The paper is organized as follows. A short description of the code and the set-up of the simulations, together with the list of parameters used are presented in Section 2. The results are given in Section 3. We discuss these results in Section 4 and Section 5 collects the conclusions of this work.

2 NUMERICAL SIMULATIONS

2.1 The code

The magnetohydrodynamical models have been computed following the approach developed by Komissarov et al. (2015). This approach is designed to study the structure of steady, axisymmetric relativistic

flows using one-dimensional time-independent simulations. The key point of the approach is the use of the *quasi-one-dimensional* approximation, which requires that the jet radius is much smaller than its length (i.e. narrow jets), and that the flow speed is close to the light speed c. Under these assumptions, together with that of negligible azimuthal velocity, the steady-state equations of relativistic magnetohydrodynamics (RMHD) can be treated as a one-dimensional (radial) problem in which the axial coordinate plays the role of the *temporal* coordinate. The code thus solves the one-dimensional time-dependent equations of RMHD plus a conservation equation for the tracer (jet mass fraction).

The use of this approach allowed us to span a wide region of the parameter space, at the cost of giving a poor description of the jet boundary where the jet flow velocity becomes subrelativistic (see e.g. Martí, Perucho & Gómez 2016; Fuentes et al. 2018). However, in this paper we focus on jet deceleration due to mass loading from stars inside the jet, a process in which the jet boundary plays no role. Besides, our approach is not suitable to describe the phase of strong jet deceleration once the flow velocity deviates significantly from the speed of light. Nevertheless, it is useful to discern the jet conditions under which the flow can or cannot be decelerated by stellar wind mass load.

2.2 Set-up

2.2.1 Jet parameters

The majority of simulated models have a total power of $L_{\rm j} = 10^{43}$ erg s^{-1}, a typical value for FR I jets, and have a radius $R_{\rm j} = 1$ pc at injection. The modelled jets are purely leptonic ($X_{\rm e} = \rho_{\rm e}/\rho = 1$). The jet density, Lorentz factor, and axial component of the magnetic field are different among models but all are considered to be initially constant across the jet. The configuration of the toroidal field is also the same for all magnetized models

$$B^{\phi}(r) = \begin{cases} \dfrac{2B^{\phi}_{\rm m,j}(r/R_{\rm m})}{1 + (r/R_{\rm m})^2}, & 0 \leq r \leq R_{\rm j} \\ 0, & r > R_{\rm j}, \end{cases} \quad (2)$$

with the same $R_{\rm m} = 0.37R_{\rm j}$ (the radius at which the toroidal magnetic field reaches its maximum, $B^{\phi}_{\rm m,j}$), but different $B^{\phi}_{\rm m,j}$. Jets are injected in pressure equilibrium with the ambient medium, by computing the pressure distribution across the jet and matching them at the boundary as in Martí (2015) and Martí et al. (2016). We have incorporated the relativistic gas equation of state of Synge (1957), using the approximation given by Choi & Wiita (2010).

In order to compute the whole set of jet parameters, we started by fixing the jet rest-mass density, Lorentz factor, mean magnetic pitch angle,[1] and ambient pressure. The jet densities, $\rho_{\rm j}$, span four orders of magnitude, from 10^{-32} to 10^{-28} g cm^{-3}; Lorentz factors, $\gamma_{\rm j}$, at injection range from 6 to 10; and mean magnetic pitch angles, $\phi_{\rm B,j}$, are 10°, 45°, and 75°. The ambient pressure at injection is $p_{\rm a,0} = 10^{-7}$ dyn cm^{-2}. With these four parameters, and having fixed the jet power and radius, the remaining parameters of the jet can be derived; in particular, the mean gas pressure, $p_{\rm j}$, axial field, $B^{z}_{\rm j}$, toroidal field $B^{\phi}_{\rm j}$, and maximum toroidal field, $B^{\phi}_{\rm m,j}$.

---

[1] We define the pitch angle as $\phi_B = \tan^{-1}(B^{\phi}/B^z)$, so that $\phi_B = 90°$ stands for a purely toroidal field, whereas $\phi_B = 0°$ stands for a purely poloidal field.

The total power of the jet, including the rest-mass energy flux, is defined as

$$L_{\rm j} = A_{\rm j} \left(\rho_{\rm j} h_{\rm j} \gamma_{\rm j}^2 + (B^{\phi}_{\rm j})^2 \right) v_{\rm j}, \quad (3)$$

where $A_{\rm j}$ is the jet cross-section ($A_{\rm j} = \pi R_{\rm j}^2$) and $h_{\rm j}$ the specific enthalpy (Choi & Wiita 2010),

$$h_{\rm j} = \frac{5c^2}{2\xi} + (2 - \kappa)c^2 \left[\frac{9}{16}\frac{1}{\xi^2} + \frac{1}{(2 - \kappa + \kappa\mu)^2} \right]^{1/2}$$

$$+ \kappa c^2 \left[\frac{9}{16}\frac{1}{\xi^2} + \frac{\mu^2}{(2 - \kappa + \kappa\mu)^2} \right]^{1/2}, \quad (4)$$

with $\xi = \rho_{\rm j}c^2/p_{\rm j}$, $\kappa = n_{\rm p^+}/n_{\rm e^-}$ the ratio of proton and electron number densities, and $\mu = m_{\rm p}/m_{\rm e}$ the ratio of proton and electron masses. We note that in all the simulated models $\kappa = 0$ at injection.

Furthermore, for the chosen configuration of the toroidal magnetic field, equilibrium with the ambient medium at injection demands that (Martí 2015)

$$p_{\rm j} = p_{\rm a,0} - \frac{(B^{z}_{\rm j})^2}{2}, \quad (5)$$

or, alternatively,

$$p_{\rm j} = p_{\rm a,0} - \frac{(B^{\phi}_{\rm j})^2}{2\tan^2 \phi_{\rm B,j}}. \quad (6)$$

Now, with $L_{\rm j}$, $\rho_{\rm j}$, $\gamma_{\rm j}$, $A_{\rm j}$, $\phi_{\rm B,j}$, and $p_{\rm a,0}$ fixed, the system formed by equations (3) and (4) (with $\kappa = 0$) and (6) is solved for $p_{\rm j}$ and the remaining parameters are derived. The mean toroidal field is

$$B^{\phi}_{\rm j} = \sqrt{2(p_{\rm a,0} - p_{\rm j})} \tan \phi_{\rm B,j}. \quad (7)$$

The (assumed constant) axial magnetic field is then $B^{z}_{\rm j} = B^{\phi}_{\rm j}/\tan \phi_{\rm B,j}$, and the maximum toroidal field is (see Martí 2015)

$$B^{\phi}_{\rm m,j} = \frac{B^{\phi}_{\rm j} R_{\rm j}^2}{4R_{\rm m}(R_{\rm j} - R_{\rm m}\arctan(R_{\rm j}/R_{\rm m}))} \quad (8)$$

($\simeq 1.23 B^{\phi}_{\rm j}$ for $R_{\rm m} = 0.37 R_{\rm j}$).

The equilibrium profile for the gas pressure within the jet is then computed as in Martí (2015). Previous work with this code (Martí et al. 2016) has shown that a contact discontinuity between the jet and the ambient medium can lead to the development of the pinching instability in axisymmetric flows and the disruption of the steady state that we require for isolating the role of mass load on jet dynamics. Therefore, a shear layer has been imposed in all the models by convolving the sharp jumps with the function sech r^m with $m = 8$ ($\Delta r_{\rm sl} \approx 0.2R_{\rm j}$) in order to provide further stability to the solutions.

2.2.2 The models

Table 1 shows the relevant parameters used in a number of the different simulations discussed in this paper. In Appendix A, we show a table with the parameters of a number of intermediate models that were also analysed and contributed to the conclusions derived.

The columns of Table 1 give the model name, jet rest-mass density, Lorentz factor, mean pitch angle, temperature, adiabatic exponent, $\Gamma_{\rm ad}$, specific enthalpy, axial magnetic field, maximum toroidal field, internal energy density, $e = \rho (h - c^2)/\Gamma_{\rm ad}$, magnetic energy density, $u_{\rm B}$, and the magnetization parameter, $\beta = u_{\rm B}/(2p)$, jet radius, power, and ambient pressure at injection, respectively. Values of h/c^2 significantly larger than 1 imply models in which the internal energy dominates over the rest-mass energy density (*hot*

Table 1. Simulation parameters.

Model	ρ (g cm^{-3})	γ	ϕ_B (°)	T (K)	Γ_ad	h (c^2)	B^z (mG)	B_m^ϕ (mG)	e (erg cm^{-3})	u_B (erg cm^{-3})	β	R_j (pc)	L_j (erg s^{-1})	$p_{\mathrm{a},0}$ (dyn cm^{-2})
J4_X	10^{-28}	10	–	5.8×10^8	1.62	1.24	–	–	1.44×10^{-8}	–	–	1	10^{43}	10^{-7}
J4_Y	10^{-28}	7	–	3.1×10^9	1.50	2.58	–	–	8.45×10^{-8}	–	–	1	10^{43}	10^{-7}
J4_Z	10^{-28}	6	–	4.6×10^9	1.46	3.47	–	–	1.56×10^{-7}	–	–	1	10^{43}	10^{-7}
J4_A	10^{-28}	10	45	5.4×10^8	1.62	1.23	1.51	1.92	1.26×10^{-8}	1.86×10^{-7}	11.4	1	10^{43}	10^{-7}
J4_B	10^{-28}	7	45	3.0×10^9	1.49	2.54	1.17	1.37	9.36×10^{-8}	1.11×10^{-7}	1.19	1	10^{43}	10^{-7}
J4_C	10^{-28}	6	45	4.6×10^9	1.45	3.49	0.87	1.06	1.55×10^{-7}	6.21×10^{-8}	0.44	1	10^{43}	10^{-7}
J4_E	10^{-28}	10	10	5.8×10^8	1.62	1.26	1.51	0.33	1.44×10^{-8}	1.84×10^{-7}	10.4	1	10^{43}	10^{-7}
J4_F	10^{-28}	7	10	3.1×10^9	1.49	2.60	1.15	0.25	9.45×10^{-8}	1.08×10^{-7}	1.14	1	10^{43}	10^{-7}
J4_G	10^{-28}	6	10	4.6×10^9	1.46	3.52	0.87	0.19	1.56×10^{-7}	5.94×10^{-8}	0.42	1	10^{43}	10^{-7}
J4_J	10^{-28}	7	75	2.4×10^9	1.52	2.17	1.28	5.77	6.93×10^{-8}	1.66×10^{-7}	2.30	1	10^{43}	10^{-7}
J4_K	10^{-28}	6	75	4.1×10^9	1.47	3.20	0.98	4.40	1.35×10^{-7}	1.04×10^{-7}	0.83	1	10^{43}	10^{-7}
J8_X	10^{-32}	10	–	1.8×10^{13}	1.33	1.21×10^4	–	–	8.48×10^{-8}	–	–	1	10^{43}	10^{-7}
J8_Y	10^{-32}	7	–	3.8×10^{13}	1.33	2.56×10^4	–	–	1.74×10^{-7}	–	–	1	10^{43}	10^{-7}
J8_Z	10^{-32}	6	–	5.2×10^{13}	1.33	3.50×10^4	–	–	2.38×10^{-7}	–	–	1	10^{43}	10^{-7}
J8_A	10^{-32}	10	45	1.8×10^{13}	1.33	1.23×10^4	1.35	1.65	8.37×10^{-8}	1.47×10^{-7}	2.63	1	10^{43}	10^{-7}
J8_B	10^{-32}	7	45	3.8×10^{13}	1.33	2.54×10^4	1.04	1.28	1.73×10^{-7}	8.79×10^{-8}	0.76	1	10^{43}	10^{-7}
J8_C	10^{-32}	6	45	5.2×10^{13}	1.33	3.49×10^4	0.74	0.91	2.37×10^{-7}	4.46×10^{-8}	0.28	1	10^{43}	10^{-7}
J8_E	10^{-32}	10	10	1.8×10^{13}	1.33	1.26×10^4	1.33	0.29	8.48×10^{-8}	1.45×10^{-7}	2.56	1	10^{43}	10^{-7}
J8_F	10^{-32}	7	10	3.8×10^{13}	1.33	2.58×10^4	1.03	0.22	1.74×10^{-7}	8.53×10^{-8}	0.74	1	10^{43}	10^{-7}
J8_G	10^{-32}	6	10	5.2×10^{13}	1.33	3.52×10^4	0.73	0.17	2.38×10^{-7}	4.30×10^{-8}	0.27	1	10^{43}	10^{-7}
J8_I	10^{-32}	10	75	1.5×10^{13}	1.33	1.02×10^4	1.37	6.46	6.86×10^{-8}	1.77×10^{-7}	3.90	1	10^{43}	10^{-7}
J8_J	10^{-32}	7	75	3.3×10^{13}	1.33	2.26×10^4	1.11	5.08	1.53×10^{-7}	1.28×10^{-7}	1.25	1	10^{43}	10^{-7}
J8_K	10^{-32}	6	75	4.9×10^{13}	1.33	3.29×10^4	0.81	3.71	2.22×10^{-7}	7.36×10^{-8}	0.50	1	10^{43}	10^{-7}
J91X	3×10^{-33}	3.2	–	3.2×10^{11}	1.33	2.13×10^2	–	–	4.28×10^{-10}	–	–	10	5×10^{41}	2.5×10^{-10}
J91D	3×10^{-33}	3.2	45	3.2×10^{11}	1.34	2.05×10^2	0.015	0.018	4.12×10^{-10}	2.45×10^{-10}	0.89	10	5×10^{41}	2.5×10^{-10}
J91H	3×10^{-33}	3.2	10	3.2×10^{11}	1.34	2.13×10^2	0.015	3.16×10^{-3}	4.28×10^{-10}	2.14×10^{-10}	0.74	10	5×10^{41}	2.5×10^{-10}
J92X	3×10^{-35}	3.2	–	3.2×10^{13}	1.33	2.14×10^4	–	–	4.31×10^{-10}	–	–	10	5×10^{41}	2.5×10^{-10}
J92D	3×10^{-35}	3.2	45	3.2×10^{13}	1.33	2.06×10^4	0.015	0.018	4.15×10^{-10}	2.45×10^{-10}	0.89	10	5×10^{41}	2.5×10^{-10}
J92H	3×10^{-35}	3.2	10	3.2×10^{13}	1.33	2.14×10^4	0.015	3.16×10^{-3}	4.30×10^{-10}	2.14×10^{-10}	0.74	10	5×10^{41}	2.5×10^{-10}

models). According to the values in the table, models range between moderately hot (or *warm*; models J4__) to hot. The values of β indicate the ratio of the jet magnetic to internal energy densities. Values of β are in the interval ~ 0.1 to ~ 10.

Fixing the jet power at injection and ambient pressure, leaves three main parameters that may be changed to define the jet configuration, namely, the jet density, which we sweep in the range 10^{-32}–10^{-28} g cm^{-3} for the main set of models, the Lorentz factor, ranging from 6 to 10, and the mean pitch angle of the magnetic field, which takes the values of $10°$, $45°$, and $75°$. Imposing transversal equilibrium fixes the rest of the jet parameters, as explained in Martí (2015) and Martí et al. (2016).

We note here that there is little chance to find an ordered poloidal field at the simulated scales as implied by simple magnetic flux conservation (see Begeleman, Blandford & Rees 1984), and from observational evidence, because the observed symmetry of the transverse brightness and polarization profiles is also inconsistent with global helical fields threading jets. Therefore, although the toroidal field component is probably ordered, the poloidal component (comparable in magnitude at the base of the flaring region, Laing & Bridle 2014) must have reversals: for instance, shear can contribute to the generation of a poloidal component across the jet's velocity gradients. Acknowledging these facts, we have simplified the set-up of the magnetic field by including such an ordered structure. Nevertheless, the poloidal fields at injection given in Table 1 (1 mG) result in a poloidal flux of 3×10^{34} Gcm^2, which compares to the estimate of 1×10^{34} Gcm^2 for a 10^9 M$_\odot$ by Begeleman et al. (1984), and is also within the order of magnitude given in Zamaninasab et al. (2014), which indicates that there is no major inconsistency between our adopted parameters and different theoretical approaches.

The names of the models provide information about their parameters. The second character, ranging from 4 to 9, gives the approximate (inverse) order of magnitude ratio between the jet density and the proton mass per cubic centimetre. Therefore, the larger the number, the smaller the density of the jet. The third character refers to the properties of the ambient medium (see Section 2.2.3 and Table 3).

The last character of the model name provides information about both the jet Lorentz factor and the magnetic field structure: For each pitch angle, the letters stand for Lorentz factor 10, 7, and 6 (in alphabetical order), as indicated in Table 1, with the Lorentz factor decreasing with the alphabetical order for a given pitch angle.

We have also run two sets of models, J91_ and J92_, with a lower power (5×10^{41} erg s^{-1}) and a larger radius (10 pc) to be compared with the purely hydrodynamical jet models A and D in Perucho et al. (2014), respectively. The parameters defining these models appear in the last part of Table 1. They are injected with the same densities (3×10^{-33} and 3×10^{-35} g cm^{-3}, respectively) and Lorentz factor (3.2) as those in models A and D in Perucho et al. (2014).

Table 2 compiles the kinetic, internal, and magnetic energy fluxes of all the models in terms of the total jet flux, L_j. Note that except for the models with the higher rest-mass densities and Lorentz factor (J4_X, J4_A, J4_E) that are kinetically dominated, all the high-power models are dominated by the internal energy flux. Note also that the largest Poynting flux jets are those with the larger magnetic pitch angle, and among them, those with the larger Lorentz factor (J5_I, J7_I, J8_I). Low-power jet models (J9) are also dominated by the internal energy flux at injection. The magnetic field configuration chosen together with the condition of transversal equilibrium imposed to our models do not allow for Poynting-flux dominated jets within the domain of the space of parameters under study.

Table 2. Kinetic (F_k), internal (F_i), and magnetic (F_p) energy fluxes as fractions of the total energy flux of the jet.

Model	F_k	F_i	F_p
J4_X	0.796	0.204	–
J4_Y	0.388	0.612	–
J4_Z	0.284	0.716	–
J4_A	0.796	0.188	0.016
J4_B	0.388	0.602	9.52×10^{-3}
J4_C	0.284	0.711	5.28×10^{-3}
J4_E	0.796	0.204	5.05×10^{-4}
J4_F	0.388	0.612	2.93×10^{-4}
J4_G	0.284	0.716	1.62×10^{-4}
J4_J	0.388	0.454	0.158
J4_K	0.284	0.624	0.092
J8_X	7.96×10^{-5}	0.99992	–
J8_Y	3.88×10^{-5}	0.99996	–
J8_Z	2.84×10^{-5}	0.99997	–
J8_A	7.96×10^{-5}	0.987	0.013
J8_B	3.88×10^{-5}	0.992	7.58×10^{-3}
J8_C	2.84×10^{-5}	0.996	3.81×10^{-3}
J8_E	7.96×10^{-5}	0.9995	3.98×10^{-4}
J8_F	3.88×10^{-5}	0.9997	2.34×10^{-4}
J8_G	2.84×10^{-5}	0.9999	1.17×10^{-4}
J8_I	7.96×10^{-5}	0.808	0.192
J8_J	3.88×10^{-5}	0.878	0.122
J8_K	2.84×10^{-5}	0.935	0.065
J91X	4.67×10^{-3}	0.995	–
J91D	4.67×10^{-3}	0.957	0.038
J91H	4.67×10^{-3}	0.994	0.001
J92X	4.67×10^{-5}	0.999	–
J92D	4.67×10^{-5}	0.962	0.038
J92H	4.67×10^{-5}	0.999	0.001

2.2.3 Ambient medium and stellar winds

A pressure profile for the ambient medium is set-up to reproduce typical galactic atmospheres and trigger the sideways expansion of the jet

$$p_a(z) = p_{a,0} \left(1 + \left(\frac{z}{r_c} \right)^2 \right)^\alpha, \qquad (9)$$

where r_c is the inner core radius. This expression corresponds to that of an isothermal atmosphere with the same density profile as used in Perucho et al. (2014). The mass loading of the jets from stellar winds is accounted for by adding a source term in the (relativistic) density conservation equation in the same way as described in Perucho et al. (2014). The mass load rate per unit volume follows

$$Q(z) = Q_0 \left(1 + \left(\frac{z}{r_{c,s}} \right)^2 \right)^{\alpha_s}, \qquad (10)$$

where $r_{c,s}$ is the stellar core radius. The composition of the injected gas is proton–electron, i.e. ionized hydrogen.

The last column of Table 1 shows the value of the ambient pressure at injection, which fixes the jet equilibrium configuration. All models were run with the same ambient pressure at injection $p_{a,0} = 10^{-7}$ dyn cm^{-2}, and the same stellar core radius, $r_{c,s} = 500$ pc and $\alpha_s = -1.095$ (see equation 10), but for the case of J9 models, where we

Table 3. Different pressure core radii, mass injection rates, and corresponding mean stellar mass-loss rates used in the simulations.

Model	r_c (kpc)	Q_0 (g y^{-1} pc^{-3})	$\dot{M}$ (M$_\odot$ yr^{-1})
J_N_	0.5	4.71×10^{21}	10^{-13}
J_O_	0.5	4.71×10^{23}	10^{-11}
J_P_	0.2	4.71×10^{23}	10^{-11}
J_Q_	0.5	4.71×10^{24}	10^{-10}
J_R_	0.5	4.71×10^{25}	10^{-9}
J_S_	0.2	4.71×10^{25}	10^{-9}

have fixed the same ambient parameters as in Perucho et al. (2014) for all models.[2]

We change two parameters to set-up the different simulations, namely, the galactic core radius in pressure, which takes the values $r_c = 500$ and 200 pc , and the fiducial mass injection rate per unit volume, which is taken as $Q_0 = 4.71 \times 10^{23}$ g yr^{-1} pc^{-3}, a value two orders of magnitude larger than the fiducial value in Bowman et al. (1996),[3] $Q_0 = 4.71 \times 10^{24}$ g yr^{-1} pc^{-3}, and $Q_0 = 4.71 \times 10^{25}$ g yr^{-1} pc^{-3}. The latter represents an extreme value of mass load, corresponding to a mean stellar mass-loss of $\sim 10^{-9}$ M$_\odot$ yr^{-1} for a stellar density of 10 pc^{-3} (see Vieyro et al. 2017). These mass loads correspond to mass injection rates that are much larger than expected for normal ellipticals. We know, from Perucho et al. (2014), that jet powers of 10^{43} erg s^{-1} are probably too high for mass input from stars to have much effect for normal elliptical hosts. Although the aim of this work is to understand the basic physics of the process and to compare the models presented here with those in Perucho et al. (2014), we have added models with $Q_0 = 4.71 \times 10^{21}$ g yr^{-1} pc^{-3} (as in Bowman et al. 1996) to discuss the effect of the expected mass load in typical elliptical galaxies on classical FR I jets. Finally, we also ran a set of models for which $Q_0 = 0$ g yr^{-1} pc^{-3} that were run as controls (the results of these models are not shown because they follow the expected behaviour and no significant features).

The combinations, along with the indication of the corresponding character at the third position of the model name, are displayed in Table 3, and give rise to five possible ambient configurations through which all models in Table 1 have been run.

In cylindrical coordinates, the numerical grid is $(r, z) \in [0, 20R_j] \times [0, 500R_j]$, with $R_j = 1$ pc in the high-power jets, and $R_j = 10$ pc in the low-power ones. The number of cells of the simulation box is $1600 \times 10\,000$, which implies a transversal resolution of 80 cells/R_j, and an axial resolution of 20 cells/R_j. Axisymmetry forces reflection boundary conditions on the jet axis. The outer boundary corresponds to the jet surface (defined as the contour line with tracer $f = 0.5$). At the boundary, the ambient pressure is set according to equation (9) at each step. Moreover, the ambient density and the ambient flow speed are reset, respectively, to the values of the rest-mass density in the lab frame and the jet flow velocity in the jet cell contiguous to the boundary, in order to avoid shocks being generated at the boundary between the jet and the ambient medium (see Komissarov et al. 2015).

---

[2]These parameters are $p_{a,0} = 2.5 \times 10^{-10}$ dyn cm^{-2} and $r_c = 1.2$ kpc, $\alpha = -1.095$ in equation (9), and $Q_0 = 4.71 \times 10^{21}$ g yr^{-1} pc^{-3}, $r_{c,s} = 260$ pc, and $\alpha_s = -0.23$ in equation (10).

[3]The aim of this work is to study the scenarios in which jets could be decelerated by stellar winds alone. In this respect, the results obtained in Perucho et al. (2014) pointed towards powerful mass-losses being required to decelerate jets with powers $\sim 10^{43}$ erg s^{-1}.

The physical size of the numerical grids has been chosen to obtain a compromise between numerical resolution, a number of simulations that covers a large region of the parameter space, and a distance within which most of the stellar mass load is expected. On the one hand, beyond 500 pc, the expected decrease in ambient density causes the jet to expand, thereby including more stars in its volume and encouraging deceleration. On the other hand, the expected drop in stellar number density would make deceleration by stellar winds more difficult, and, in addition, a hot jet is still expected to accelerate as it expands or by buoyancy. In conclusion, we expect the stronger deceleration by stellar winds to take place where the stellar density is larger, i.e. at the galactic core.

2.3 Summary on model names

A given model presented in this paper is thus defined in Tables 1 and 3, with the second character of the model's name related to the jet rest-mass density at injection, and the fourth character to both the Lorentz factor and pitch angle. These parameters can be found in Table 1. In contrast, the third character of a model's name is related to the ambient properties, which can be found in Table 3. The full information of the jet can thus be obtained by checking both tables.

As an example, the jet properties of models J4OA and J8RA can be found in Table 1 under the J4_A and J8_A names (the empty space is left for the ambient character), which are shared by all models that have those same characters but are run within different ambient properties; and these can be found in Table 3 with the corresponding letter (J_O_ and J_R_ in each case).

3 RESULTS

As an example, Fig. 1 shows, from top to bottom, the 2D distributions of logarithm of the rest-mass density, gas pressure, Lorentz factor (plus poloidal streamlines), toroidal, and axial field components, which define the steady-state solutions for model J4OA (see Appendix A2 for the case of model J4OC). These images are representative of the results obtained for each model, which will be discussed later in the paper. Note that the ambient medium is set a priori in these simulations and it is only used as a boundary condition for the computed transversal equilibrium structure.

We interpret our results in the context of the interplay between jet expansion (as they propagate through a pressure decreasing atmosphere), the subsequent cooling and acceleration (according to Bernoulli's law), the magnetic tension (which tends to avoid the jet expansion), and the loading of mass (which increases as the jet expansion and tends to decelerate the jet). Since all our models have dynamically unimportant Poynting fluxes, we do not expect magnetic acceleration to play an important role.

3.1 Low mass load in low-power jets. Comparison with RHD simulations

In Perucho et al. (2014), the authors found that a difference of one order of magnitude in the value of the fiducial mass-load rate, Q_0, could completely change the dynamics of the jets. In that paper, models C and D had the same initial conditions but different value of Q_0, which was one order of magnitude larger in model C. The hydrodynamical simulations showed that model D propagated with fairly constant radius and a minor deceleration, despite the entrainment, which only forced the cooling of the flow with distance (see fig. 11 in that paper). In this model, the velocity in the jet dropped from 0.95 ($\gamma \approx 3.2$) to 0.83c ($\gamma \approx 1.8$) within the inner
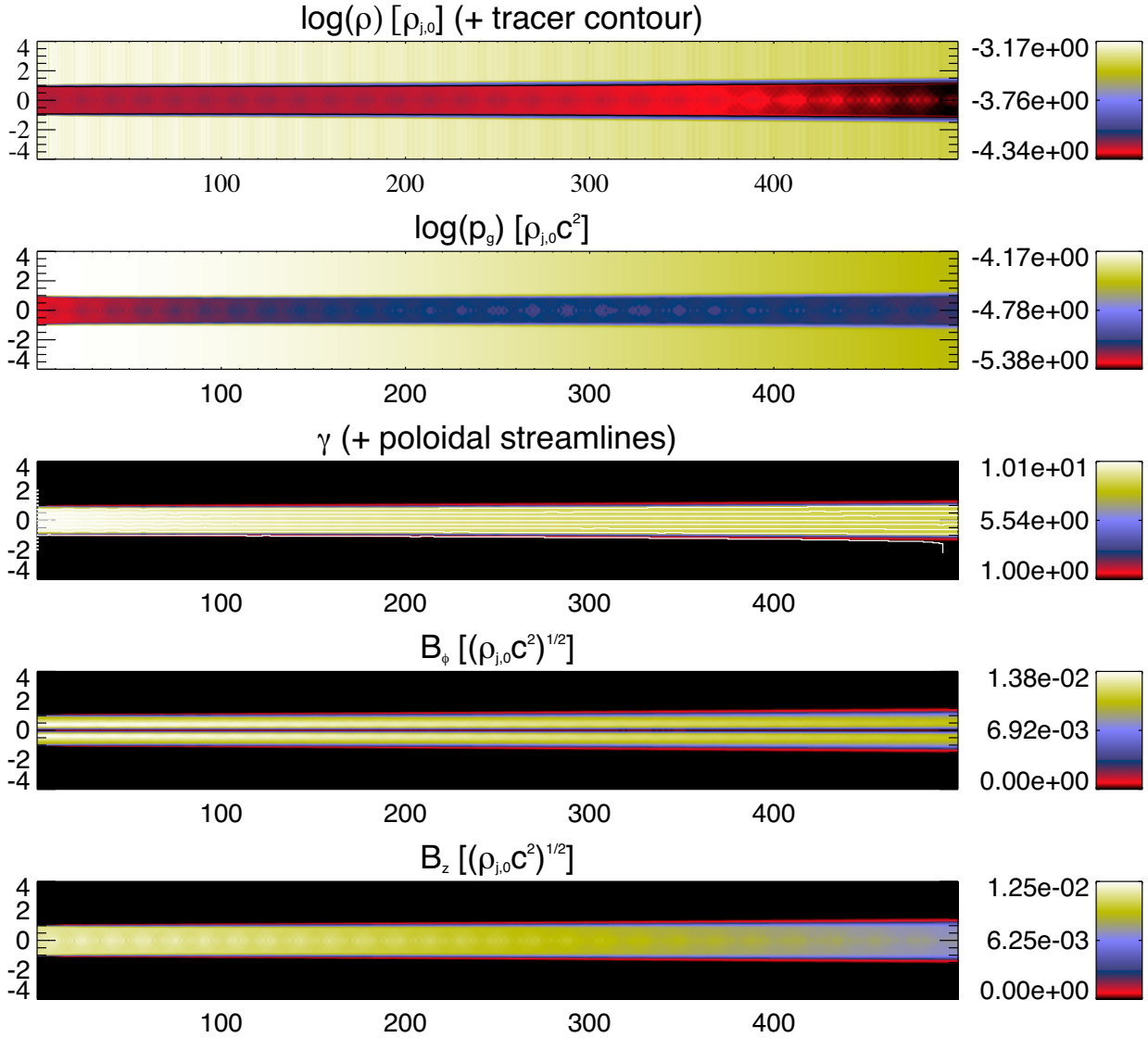
Figure 1. 2D maps of the logarithm of rest-mass density and gas pressure, Lorentz factor (including streamlines), toroidal, and axial field components for model J4OA. The units for all plots are code units (in which unit density is $\rho_{j,0} = 1$, unit distance is the jet radius $R_{j,0} = 1$, and $c = 1$).

tens of parsecs after injection and oscillated around this value due to successive expansions and recollimations. In contrast, model C expanded and was efficiently decelerated and ultimately disrupted by the growth of a pinching Kelvin–Helmholtz instability.

Models J91 and J92 have been run with specific ambient parameters (see Table 3) to be compared with the purely hydrodynamical models presented in Perucho et al. (2014). In particular, they were run with the same mass load as model D in that paper.

Fig. 2 shows the evolution with distance of the jet radius, and the averages of the jet rest-mass density, flow Lorentz factor, and magnetization, for magnetized jets with pitch angles $\phi_B = 45°$ (model J91D) and $10°$ (J91H), and for pure hydrodynamical jets (J91X). Models with $\phi_B = 75°$ could not be run because no equilibrium solution could be found for them. The plotted values are obtained as volume weighted means across the jet, bounded by the surface with jet mass fraction $f = 0.5$, which is the reason why, for instance, the mean values of the jet Lorentz factors at injection are below their values on axis. In these very low density models, moreover, the jet density is dominated by the mass loading from the first numerical

cell. This explains the discrepancy between the first rest-mass density values in the plots and the injection values given in Table 1. The plots show a mild deceleration of the flow within the inner 500 pc, and an acceleration farther downstream. The jets expand with relatively small opening angles ($\approx 0.5°$). The jet density grows very fast up to 500 pc, stalls at about this distance and slowly falls thereafter. Finally, the magnetization falls in all the models due to expansion, which forces a drop in magnetic pressure, in parallel to a slowed down decrease in thermal pressure (due to the dissipation of kinetic energy and the injection of particles) induced by the mass load. The corresponding plots for models J92 are not shown because of their similarity to those for J91.

A comparison between the quasi-one-dimensional (q1D, from now on) equilibrium models J91 and J92 and the aforementioned model D shows several differences:

(i) In model D, the jet radius oscillates around the initial value, whereas it grows monotonically in models J91/J92;
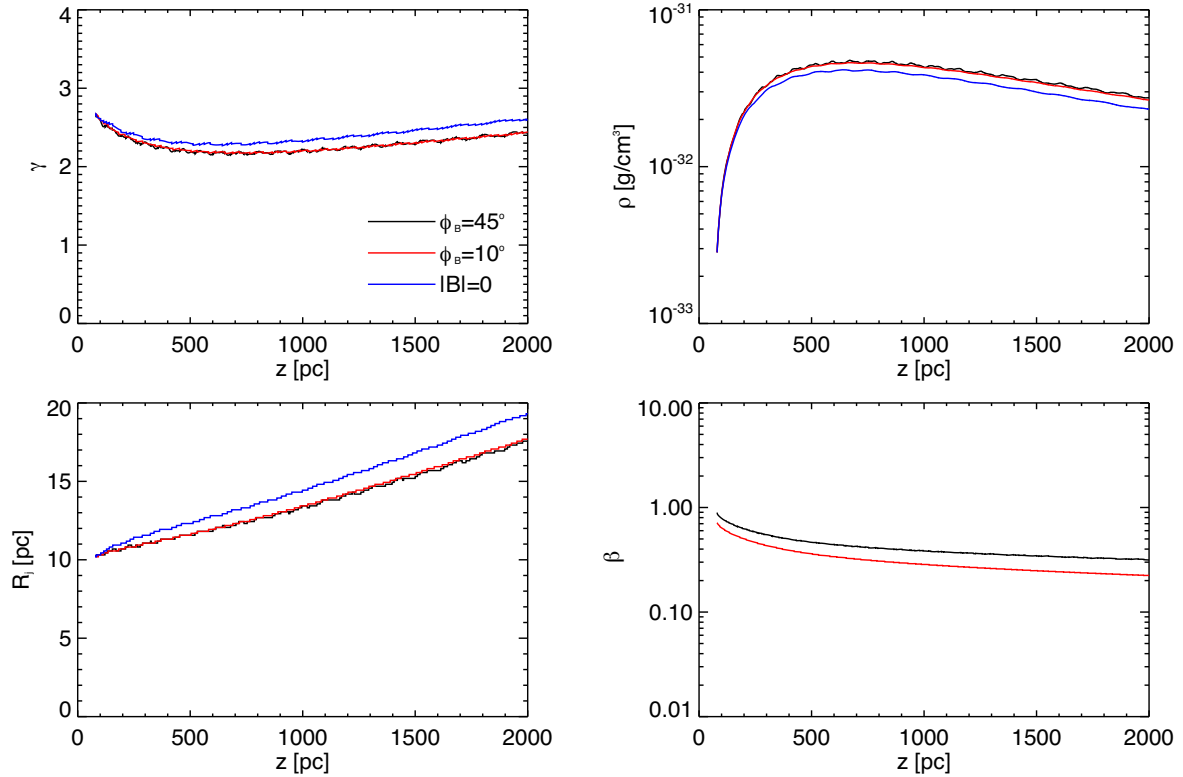
Figure 2. Mean jet Lorentz factor (top left), rest-mass density (top right), radius (bottom left), and β parameter (bottom right) versus distance for models J91. In each plot, the black, red, and blue lines represent the jets with mean pitch angles $\phi_B = 45°$ (model J91D), $10°$ (J91H), and hydro jets (J91X), respectively.

(ii) The jet velocity remains fairly constant in model D (in models J91/92, the jet flow accelerates once the mass load drops beyond r_s);

(iii) Pressure in model D oscillates around some equilibrium value developing a pinched structure along the jet;

(iv) The mean jet density in model D grows to values that are one order of magnitude larger than in q1D models.

These changes in behaviour result from differences in the way in which jets and ambient medium interact in the two types of simulation. While hydrodynamical model D evolved through a dynamic ambient medium formed by the shocked jet gas (the jet's cocoon), and this medium was overdense and overpressured with respect to the jet (see e.g. figs 8 and 11 in Perucho et al. 2014), q1D models J91/J92 evolve in pressure equilibrium with their environment (see Section 2). As a consequence, the ambient pressure gradient directly affects the jets in the q1D simulations, whereas the dynamical jets evolve completely embedded within their cocoons, with a fairly homogeneous pressure. This enables us to explain differences (i)–(iii) above. The higher densities attributed to model D with respect to q1D models J91/J92 (point iv above) are an artefact of the definition of the jet surface which in the case of model D comprised a wider section of the jet/ambient shear layer than in models J91/J92. It is interesting to remark that the steady-state simulations can be more representative of late time evolution, after the cocoon has evolved.

Fig. 2 shows that the purely hydrodynamical q1D jets, J91X (blue lines), undergo a slightly stronger acceleration than their magnetized counterparts as they propagate. At the same time, the rest-mass density is also slightly smaller in those models than in the magnetized ones. The relative extra acceleration and drop in rest-mass density of the hydrodynamical model are related to the extra expansion as compared to the magnetized counterparts (see Table 1).

We do not find strong differences among the magnetized models, which is common to all the simulations presented in this work. The reason is the relatively small dynamical significance of the magnetic fields with respect to either the initial fluxes of kinetic and internal energy (see Tables 1 and 2) or because of the rapid increase of kinetic energy due to mass load in hot, dilute jets. The latter option implies that the jet becomes rapidly dominated by the kinetic energy flux, making the magnetic energy flux negligible.

3.2 Moderate mass load

In this section, we focus on the role of the magnetic field and its pitch angle on jets undergoing a moderate mass load (characterized by a mass-load rate at injection of $Q_0 = 4.71 \times 10^{23}$ g yr^{-1} pc^{-3}) by a stellar population with a mean mass-loss of 10^{-11} M$_\odot$ yr^{-1}. With this aim, we present the results obtained for models J4O and J8O (four orders of magnitude lighter), which are representative limits of the parameter space we have studied. We consider magnetized models with different magnetic pitch angles ($\phi_B = 10°$, $45°$, and $75°$) and equivalent models without magnetic fields, as well as models with different Lorentz factors. Finally we compare our results with those obtained for models J4P and J8P, in which a change in the ambient pressure profile is introduced, to study the role of jet expansion induced by an earlier drop in ambient pressure. In order to facilitate the comparison among models, we use the same colour lines for the models with the same pitch angle in each of the plots.

In the absence of mass loading, hydrodynamical jets embedded in an atmosphere with decreasing pressure expand, rarify, accelerate, and cool down following Bernoulli's principle. When a jet is mass loaded, its pressure tends to decrease more slowly as a result of the dissipation of kinetic energy and the injection of particles, which
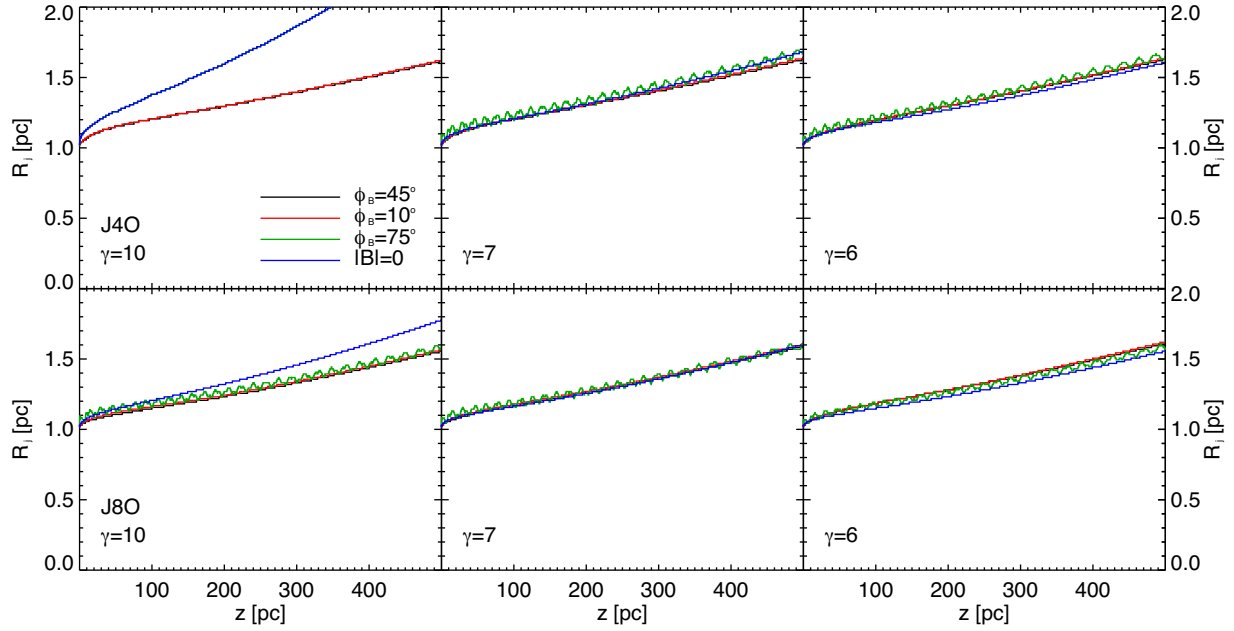
Figure 3. Jet radius versus distance for models J4O_ (top panels) and J8O_ (bottom panels). Each panel contains all the models with the same initial Lorentz factor. The left-hand panels show the models with $\gamma = 10$ (models A, I, E, X), the central panels show those with $\gamma = 7$ (models B, J, F, Y), and the right-hand panels show those with $\gamma = 6$ (models C, K, G, Z). In each plot, the black, red, green, and blue lines represent the jets with mean pitch angles $\phi_B = 45°$ (models A, B, C), $10°$ (E, F, G), $75°$ (I, J, K), and purely hydro models, respectively.

together force a faster expansion. Mass load both increases the jet density and decelerates the jet flow, while temperature increases due to kinetic energy dissipation and decreases due to the injection of cold particles, so the resulting trends will depend on the initial distribution of parameters, with cold, fast jets possibly being heated and hot jets being cooled. The picture is completed when we consider the role of the magnetic field. In magnetized jets, the magnetic tension in the radial direction (caused by the toroidal component of the magnetic field) prevents rapid expansion. On the one hand, this favours a slower conversion of the internal energy into kinetic energy but, on the other hand, it delays the deceleration by mass loading. Finally, significant magnetic acceleration would also be possible in strongly magnetized jets under the appropriate conditions.

Figs 3–6 show, respectively, the evolution of the jet radius, rest-mass density, flow Lorentz factor, and temperature along the simulated grid (0.5 kpc long) for models J4O and J8O. The radii of the jets as a function of distance are shown in Fig. 3. All the jets expand as they propagate. The role of the magnetic tension in counterbalancing jet expansion is visible for the magnetized, $\gamma = 10$ jets (models J4OA, J4OE, J8OA, J8OE, J8OI) when compared with the corresponding, purely hydrodynamical ones (J4OX, J8OX, left column of Fig. 3). The enhanced expansion seen in model J4OX is the result of the efficient conversion of kinetic energy into internal energy in this non-magnetized, kinetically dominated jet model.

The evolution of jet radius, rest-mass density, and flow Lorentz factor along the jets are related by mass conservation (including the loaded mass). Rest-mass densities for models J4O and J8O are shown in Fig. 4. Magnetized models J4O undergo an increase in the rest-mass density along the first tens of parsecs from the mass loading followed by a gentle decrease governed by the jet expansion (and the decrease of the mass-load rate with distance). In the case of model J4OX, the jet expansion is so fast that the density decreases right from the jet base. Finally, the density in models J8O is so small that

it is dominated by the injected mass and keeps growing as the jet propagates.

Independently of the jet's initial density, $\gamma = 10$ magnetized models tend to decelerate slightly, whereas $\gamma = 6, 7$ models tend to a constant Lorentz factor (see Fig. 5). For J4O models, this can be understood if the mass load has a marginal or negligible effect on jet deceleration in these cases. For instance, in the case of the $\gamma = 10$ models J4OA and J4OE, the kinetic flux dominates over both the internal energy and the magnetic energy fluxes at injection (Table 2) and mass entrainment seems to dissipate part of the kinetic energy flux, causing the mean jet temperature to increase slightly, as shown in Fig. 6 (top left panel). In contrast, in the case of J8OA and J8OE models, the slight decrease in the jet Lorentz factor can be assigned to the strong mass load, compensated by expansion and cooling. In models with smaller Lorentz factors at injection (models J4OB, C, F, G, J, K; top central and top right panels in Figs 3–6) the dominating energy flux is that of the internal energy (Table 2), which allows the jet to keep an almost constant Lorentz factor even if considerably mass loaded, at the expense of a drop in the internal energy flux.

Although the injected mass load does not decelerate the jets, the increase of density in J8O models (see Fig. 4, bottom panels) implies a strong change in jet composition, leading to a baryonically dominated flow, with leptonic mass fraction changing from $X_e = 1$ at injection to $X_e = 10^{-3} - 10^{-2}$. On the contrary, J4O models barely change their composition, with $X_e \simeq 0.95$ at $z = 500$ pc.

The figures also reveal that for the largest pitch angle ($\phi_B = 75°$, green lines), the toroidal field triggers small-scale oscillations (pinching) at the jet boundary, which can be observed in all the plots. The reason for this is that the equilibrium solutions found for this pitch angle are already neighbouring non-equilibrium configurations in the parameter space (see Martí 2015).

A change in the pressure profile was introduced in order to check the role of an extended mass load region ($r_{c, s} = 500$ pc) within a
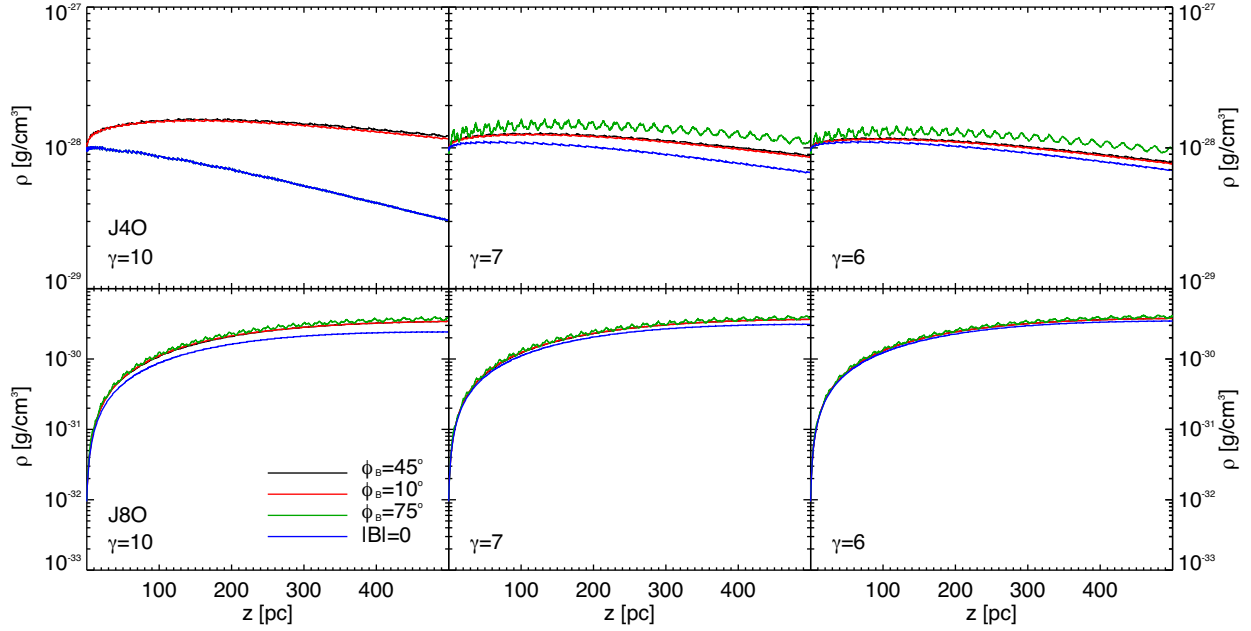
Figure 4. Mean jet rest-mass density versus distance for models J4O_ (top panels) and J8O_ (bottom panels). See the caption of Fig. 3.
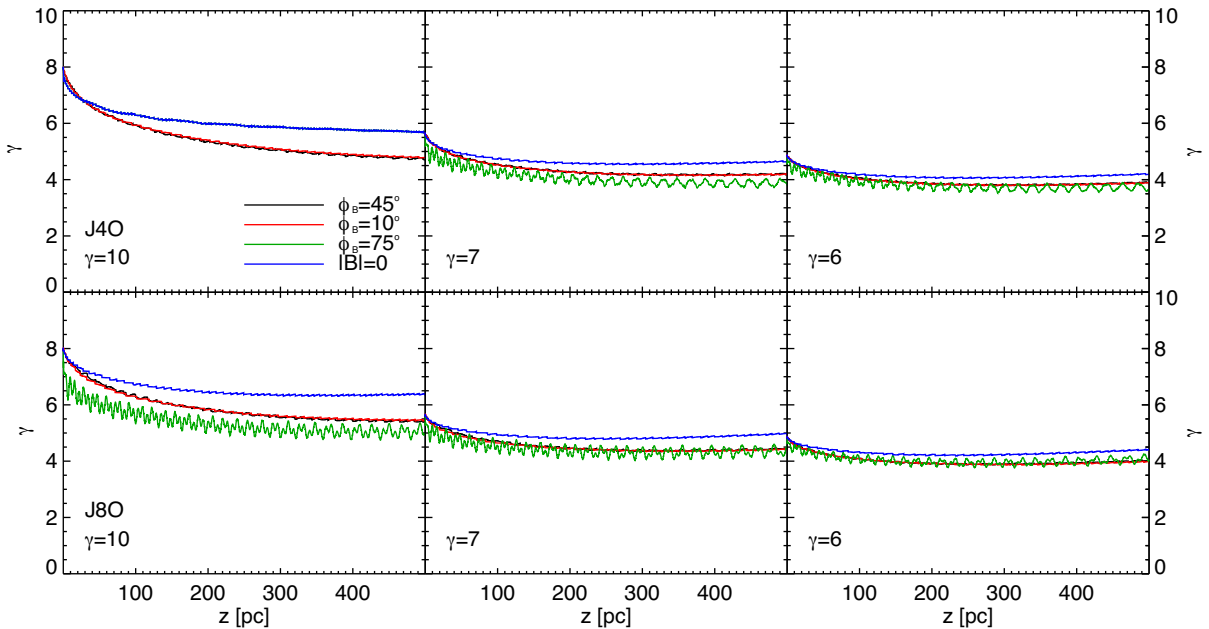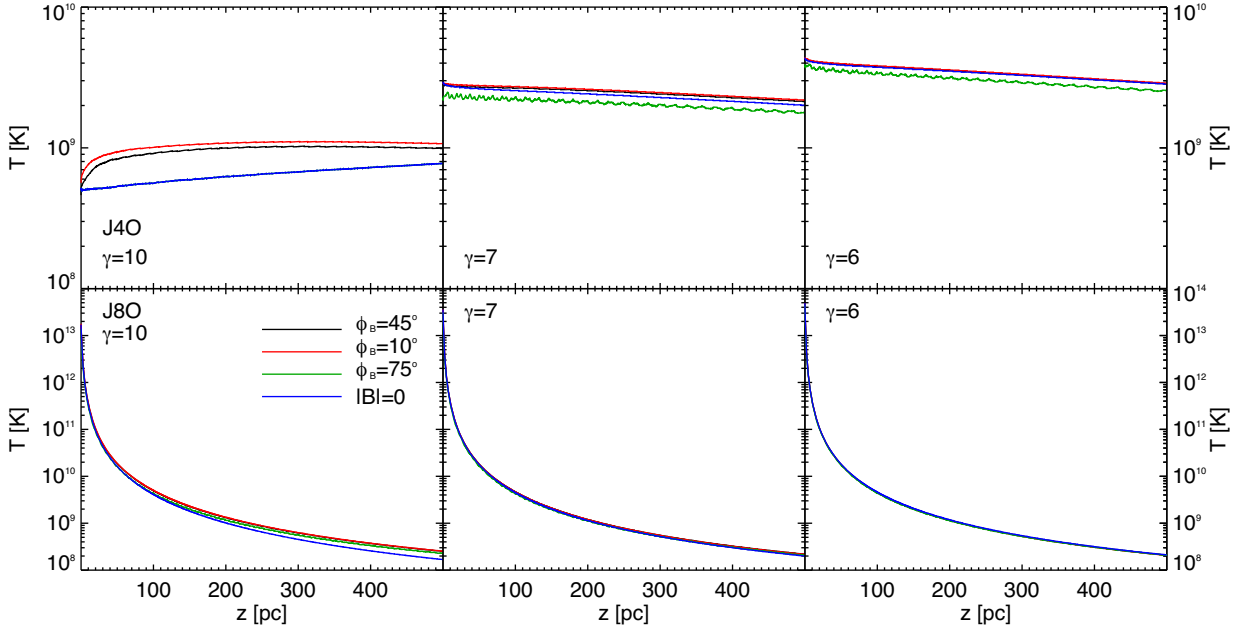

Figure 5. Mean jet Lorentz factor versus distance for models J4O_ (top panels) and J8O_ (bottom panels). See the caption of Fig. 3.

falling pressure profile from $r_c = 200\,\mathrm{pc}$ (J_P_ models). The results of models J4P (top panels) and J8P (bottom panels) are displayed in Figs 7–9. The drop in pressure favours jet expansion, which is counterbalanced by magnetic tension in magnetized jets, but not in purely hydro jets, which therefore show the largest differences in evolution (see Fig. 7). Now, in the case of denser jets, the wider local opening angle of models J4P with respect to models J4O favours the flow acceleration in the former. However, this acceleration is compensated by the increased mass load and the enhanced dissipation of kinetic energy in $\gamma = 10$ models (see top panels of Fig. 9). In the case of dilute, hot models J8P, the increased opening angle favours the conversion of internal into kinetic energy via the Bernoulli effect

and thus, jet acceleration, despite the increase in jet density (see bottom panels of Fig. 9).

3.3 Intermediate and strong mass loads

In this section, we present the results of the simulations of jets with mass-load rate at injection $Q_0 = 4.71 \times 10^{24}\,\mathrm{g\,yr^{-1}\,pc^{-3}}$ (equivalent to a mean stellar mass-loss rate of $10^{-10}\,\mathrm{M_\odot\,yr^{-1}}$ for a stellar density of $10\,\mathrm{pc^{-3}}$) in Appendix A3, Figs A3–A6, on the one hand, and also for jet models with $Q_0 = 4.71 \times 10^{25}\,\mathrm{g\,yr^{-1}\,pc^{-3}}$ (equivalent to a mean stellar mass-loss rate of $10^{-9}\,\mathrm{M_\odot\,yr^{-1}}$ for a stellar density of $10\,\mathrm{pc^{-3}}$).
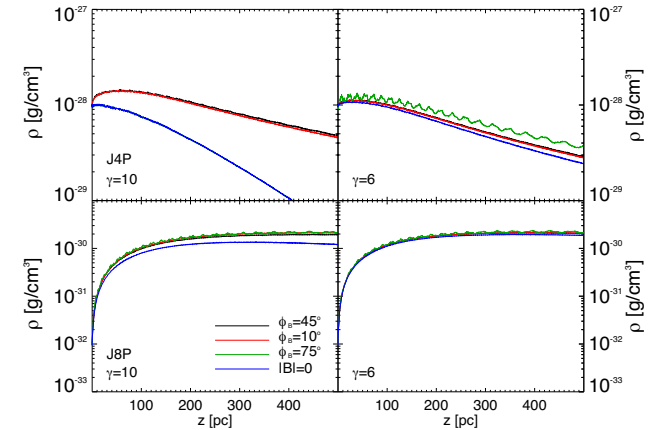
Figure 6. Jet temperature versus distance for models J4O₋ (top panels) and J8O₋ (bottom panels). See the caption of Fig. 3.
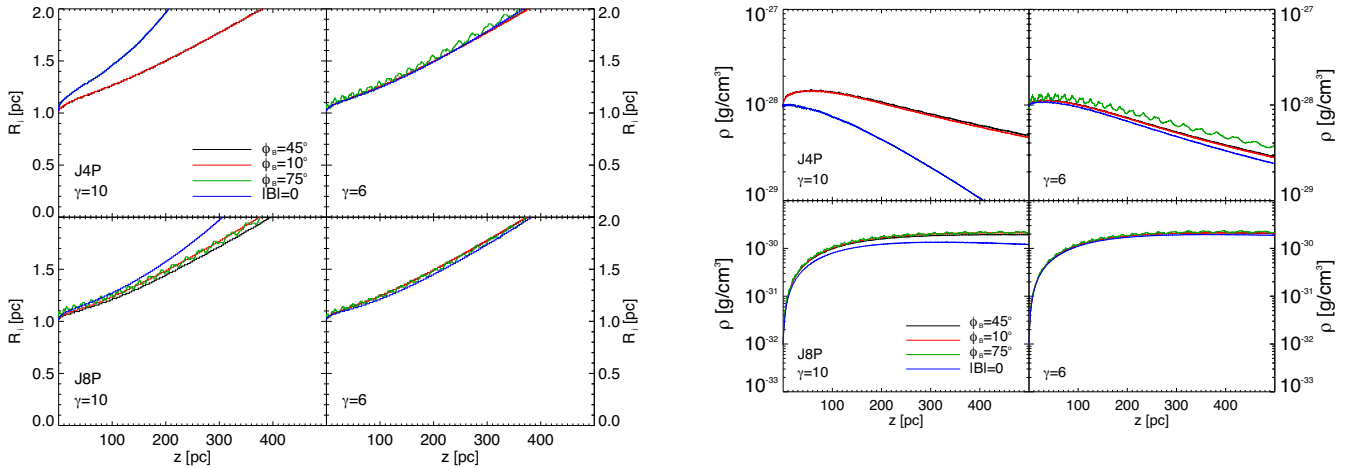
Figure 7. Jet radius for models J4P₋ (top panels) and J8P₋ (bottom panels) with Lorentz factor 10 (left column), and 6 (right column). In each plot, the black, red, green, and blue lines represent the jets with mean pitch angles ϕ_B = 45°, 10°, 75°, and purely hydro models, respectively.

Figure 8. Rest-mass density versus distance for models J4P₋ (top panels) and J8P₋ (bottom panels) with Lorentz factor 10 (left column), and 6 (right column). In each plot, the black, red, green, and blue lines represent the jets with mean pitch angles ϕ_B = 45°, 10°, 75°, and purely hydro models, respectively.

As the mass-load rate increases, a stronger deceleration in the jet flow is expected. At this point it is interesting to recall that our approach to obtain the stationary models is not valid once the flow reaches subrelativistic speeds (e.g. $\gamma \leq 2$) and therefore the subsequent jet properties are not reliable. Among the models in this set, model J4QX (purely hydrodynamical, fast and light) suffers a fast expansion and a sudden deceleration leading to a flow Lorentz factor $\gamma < 2$ beyond $z \approx 200$ pc. This result has to be taken as evidence for efficient jet deceleration. However, no valid conclusion about the subsequent evolution can be derived, beyond acknowledging that the jet is efficiently decelerated and tends to becoming subrelativistic and transonic.

Models Q expand faster than corresponding models O. At $z = 500$ pc, all Q models have a jet radius well above 2 initial jet radii whereas O models have a radius below this value (with the exception

of the pure hydrodynamical model J4OX). This is probably caused by the dissipation of kinetic energy (enhanced in the intermediate mass-load models), which produces heating, an increase of internal jet pressure, and then expansion. Moreover, there is a big difference between the local jet radius of the hydrodynamical models Q and their corresponding magnetized counterparts caused by the lack of a collimating, toroidal field in the purely hydrodynamical models. This is more striking in the case of the fastest $\gamma = 10$ cases, J4QX, J8QX, where the kinetic energy budget available for dissipation is larger.

The rest-mass density profiles of models 4Q are almost identical to those of models 4O (with the only exception of the purely hydrodynamical model J4QX). In models 4Q, the rest-mass density increases from the injection point dominated by the load of mass, reaches a maximum at $z \leq 100$ pc and then decreases dominated
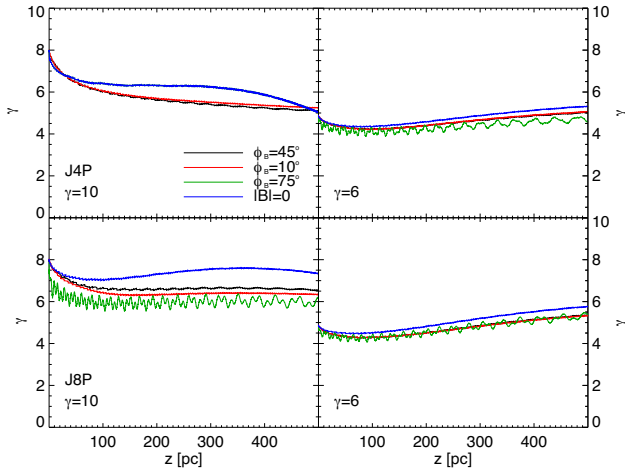
Figure 9. Mean jet Lorentz factor versus distance for models J4P$_-$ (top panels) and J8P$_-$ (bottom panels) with Lorentz factor 10 (left column), and 6 (right column). In each plot, the black, red, green, and blue lines represent the jets with mean pitch angles $\phi_B = 45°$, $10°$, $75°$, and purely hydro models, respectively.

by the jet expansion. In the lighter models 8Q (as it was in models 8O), the rest-mass density profile is dominated by the mass load and keeps growing until $z = 500$ pc despite the jet expansion. The only difference between the rest-mass density profiles of models 8Q and 8O is quantitative and reflects the difference in one order of magnitude between the mass-load rates of the two sets of models.

Unlike models O (with a moderate mass-load rate), models Q experience a strong deceleration down to Lorentz factors $\simeq 3$ with the already commented exception of the purely hydrodynamical model J4QX, which reaches $\gamma \approx 2$ at $z \approx 200$ pc, and to a less extent, J8QX, reaching $\gamma \approx 2$ at $z \approx 400$ pc. The strong deceleration experienced by models Q in comparison with models O is due to the larger mass-load rate of the former. The even stronger deceleration seen in the fast models J4QX and J8QX is the result of the enhanced dissipation of kinetic energy in these models as compared with the magnetized models or the purely hydrodynamical ones with smaller Lorentz factors at injection. In the case of the magnetized models, the presence of a collimating magnetic field prevents the expansion of the jet and therefore reduces the mass loading. In the case of hydro jets with smaller Lorentz factors, the kinetic energy dissipation is not so strong as to increase the jet pressure because of the smaller relative initial kinetic energy budget, forcing further jet expansion and more entrainment.

Fig. 10 shows the 2D distributions corresponding to the steady-state models J8RA (Lorentz factor 10 at injection; see the Appendix A2 for the case of J8RC, with Lorentz factor 6 at injection). The linear plots showing the mean jet Lorentz factor, rest-mass density, jet radius, and temperature versus distance for simulations J4R$_-$ and J8R$_-$ are shown in Appendix A3, Figs A7–A10. In contrast to the corresponding models O shown in Figs 1 and 3–6, models R show larger opening angles and stronger decelerations. In fact all these heavily mass-loaded model jets reach the limiting Lorentz factor 2 at around 100 pc, and significantly closer to the injection point, $z \approx 30$ pc, in the case of the pure hydrodynamical, $\gamma = 10$, models. In the magnetized models, the sideways expansion of the jet finds the opposition of the radial component of the magnetic tension hence reducing the expansion rate, and correspondingly the entrained mass. The result is a delayed deceleration.

4 DISCUSSION

4.1 Magnetization

Fig. 11 shows the mean magnetization, β, for models J4 (top panels) and J8 (bottom panels) with Lorentz factor 10 for moderate (models O; left-hand panels) and heavy mass-load rates (models R: right-hand panels).[4] The magnetization falls faster in models where the deceleration is also faster (i.e. those with a higher mass-load rate) and, within them, those with a smaller magnetic pitch angle. Let us try to understand these trends with the help of the following expression for β

$$\beta = \frac{(B^\phi)^2}{2p} \left(\frac{1}{\gamma^2} + \frac{1}{\tan^2 \phi_B} \right), \qquad (11)$$

where the first term in the brackets accounts for the toroidal magnetic field in the jet reference frame and the second term for the contribution of the axial field. According to it, there are obvious differences in the evolution of the magnetization between jets in which $\gamma \to 1$ due to deceleration, and those that accelerate or keep a constant velocity, and between those with large and small widening of the magnetic pitch angle along the evolution. Before proceeding, let us recall that the information derived from strongly decelerated jet simulations should be used with caution when γ approaches one.

If the jet is strongly decelerated, the first term in brackets grows to 1 and the second term tends to zero as the jet expands and $\phi_B \to 90°$. Thus, the expected trend will be that β tends to $(B^\phi)^2/(2p)$ in those cases, which results in

$$\beta \approx \frac{(B_0^\phi)^2 \, R_{j,0}^2}{2p \, R_j^2} \qquad (12)$$

(where B_0^ϕ and $R_{j,0}$ are the average toroidal magnetic field and the jet radius at $z = 0$, respectively). Note that p falls with distance unless dissipation is significant, thus partially compensating the increase in R_j with distance.

In the case of jets that are not decelerated by mass entrainment and thus $\gamma^2 \gg 1$, the dominating term in equation (11) is $1/\tan^2 \phi_B$.[5] Therefore, we have

$$\beta \approx \frac{(B^\phi)^2}{2p \, \tan^2 \phi_B} = \frac{(B^\phi)^2}{2p \, (B^\phi/B^z)^2}$$

$$= \frac{(B^z)^2}{2p} \approx \frac{(B_0^z)^2 \, R_{j,0}^4}{2p \, R_j^4}, \qquad (13)$$

where B_0^z is the axial magnetic field at injection. This is valid while the Lorentz factor of the jet is relatively large and jet expansion is not strong (when R_j grows and γ tends to one, the relation between terms in equation 11 would change). The stronger dependence on R_j ($\beta \propto 1/(p \, R_j^4)$) explains the continuous fall of the magnetization with distance observed in the left-hand panels of Fig. 11, despite the fall of p with distance.

As stated above, a direct consequence of the relative increase in p that follows entrainment in cold and fast jets (e.g. because of the dissipation of kinetic energy) is the fall of β to smaller values. Figs 12 and 13 show this effect by comparing the evolution of the magnetization for J4 and J8 models, respectively, with Lorentz

---

[4]Models with Lorentz factors 7 and 6 show equivalent behaviours, albeit with different initial values of β.

[5]In our simulations, $1/\gamma^2$ ranges between 0.01 and 0.03 at injection, whereas $1/\tan^2 \phi_B$ ranges between 0.3 and 32 for the selected initial pitch angles.
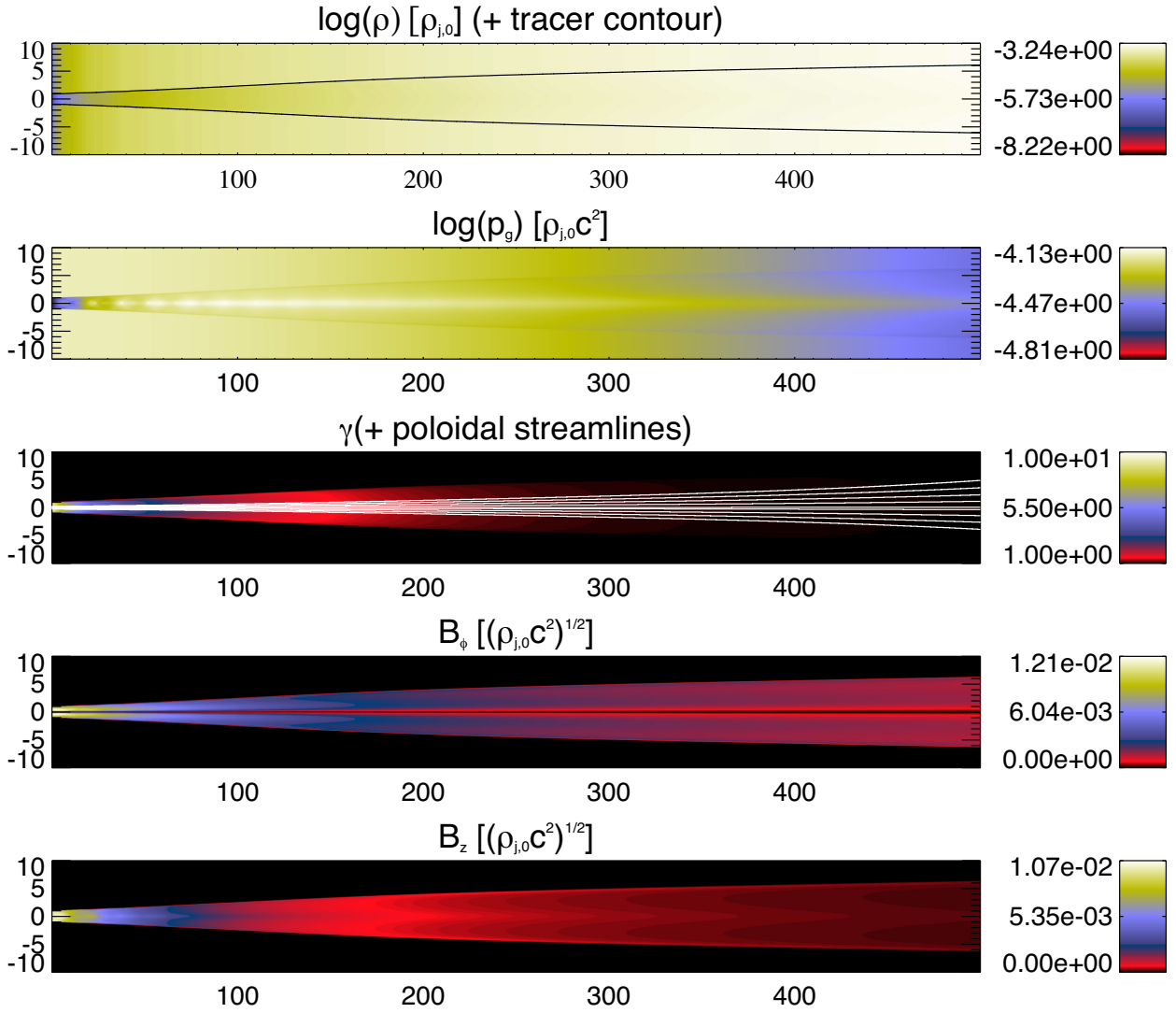
Figure 10. Same as Fig. 1 for the case of model J8RA. The units for all plots are code units (in which $\rho_{j,0} = 1$, $R_{j,0} = 1$, and $c = 1$).
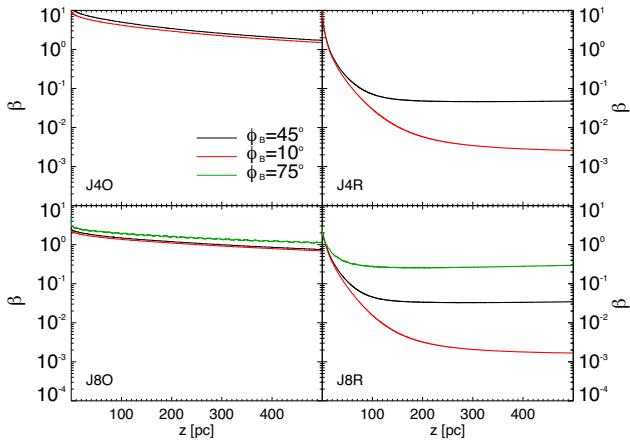


Figure 11. Mean magnetization parameter, β, for models J4O and J4R, from left to right (top panels), and J8O and J8R (bottom panels) with Lorentz factor 10. In each plot, the black and red lines represent the jets with mean pitch angles $\phi_B = 45°$ and $10°$.
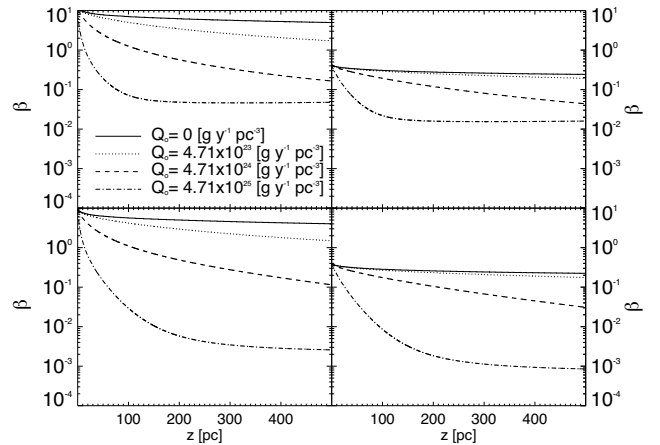
Figure 12. Mean magnetization parameter, β, for models J4, with Lorentz factor 10 (left-hand panels) and Lorentz factor 6 (right-hand panels), and pitch angles of $45°$ (top panels) and $10°$ (bottom panels). In each plot, solid, dotted, dashed, and dash–dotted lines represent the models without mass load, moderate, intermediate, and heavy mass load, respectively, for each Lorentz factor.
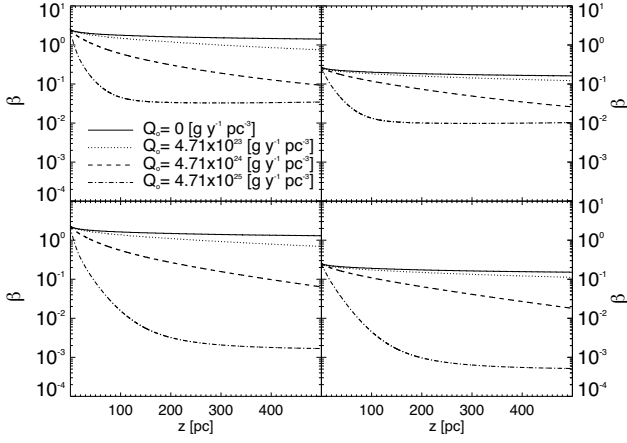
Figure 13. Mean magnetization parameter, β, for models J8, with Lorentz factor 10 (left-hand panels) and Lorentz factor 6 (right-hand panels), and pitch angles of $45°$ (top panels) and $10°$ (bottom panels). In each plot, solid, dotted, dashed, and dash–dotted lines represent the models without mass load, moderate, intermediate, and heavy mass load, respectively, for each Lorentz factor.
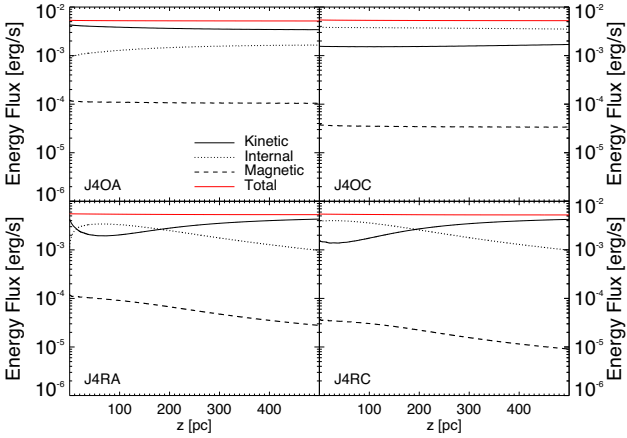
Figure 14. Energy fluxes for models J4OA (top left), J4OC (top right), J4RA (bottom left), and J4RC (bottom right), i.e. J4 models with Lorentz factors 10 (left) and 6 (right) and with moderate (top) and heavy (bottom) mass load. The red line stands for the total flux, the dotted line for the internal energy flux, the solid line for the kinetic energy flux, and the dashed line for the magnetic energy flux.

factors 10 (left-hand panels) and 6 (right-hand panels) and pitch angles $\phi_B = 45°$ (top panels) and $10°$ (bottom panels), for no mass load (purple lines), moderate mass load (solid black or red lines), and strong mass load (dashed black or red lines). The figures show that the magnetization falls faster in the Lorentz factor 10 jets, because dissipation is more relevant in this case. The effect is visible even for the case of moderate mass-load values.

Altogether, we can conclude that mass load, even if relatively small, contributes to the fall of magnetization at large distances.

4.2 Magnetic acceleration

An interesting effect is observed in a number of the simulated models, related to the conversion of Poynting flux into kinetic energy flux. In those models where the radius does not grow linearly with z, we observe a drop in Poynting flux and an extended deceleration distance as compared to purely hydro jets. Figs 14 and 15 show,

respectively, the energy fluxes for a selection of models J4 and J8 with different flow Lorentz factors, magnetic pitch angles, and mass-load rates. From the evolution of the radius with distance for the cases shown in these figures (see Figs 3 and A9), we observe that a non-linear expansion of the jet (such as the one seen in models J4RC, J8RA, J8RC, J8RI) relates to a drop in the magnetic (Poynting) flux. However, because the jets showing non-linear expansions are heavily mass loaded, the flow does not accelerate. Instead, the magnetic field acts in two different ways to extend the deceleration zone. On the one hand, the magnetic tension slows the radial expansion, thus allowing the high internal energy in these models (J8) to be slowly transferred into kinetic energy, via Bernoulli, as opposed to hydro jets (for which a faster expansion implies a faster transfer of the internal energy and a faster mass load). On the other hand, the drop in magnetic energy necessarily implies an increase in kinetic energy (in ideal RMHD), thus delaying the deceleration of the jet. Nevertheless, we recall that this effect is seen in the more strongly decelerated models and the results should be treated with caution when γ approaches one.

4.3 The dynamical role of mass load

Mass conservation in a steady relativistic flow (with $v \simeq c$) is given approximately by $\rho \gamma R_j^2 c = $ constant in the absence of mass load. If there is some mass loading, the equivalent expression can be written as

$$\rho \gamma R_j^2 v = \rho_0 \gamma_0 R_{j,0}^2 c + Q R_j^2 \Delta z, \tag{14}$$

where subscript 0 stands for injection values, the left-hand side of the equation gives the mass flux at some point downstream, Q represents the mean mass-load rate, and Δz is the distance over which the jet is mass loaded.

Therefore, the (approximate) minimum value of rest-mass density in the jet's reference frame for its mass flux not to be dominated by the mass-load, i.e. for the jet not to be decelerated to subrelativistic speeds, can be obtained by equating the two terms on the r.h.s. of equation (14), and expressed as

$$\rho_0 \gamma_0 > 6.7 \times 10^{-27} \left(\frac{\dot{M}}{10^{-11} M_\odot \mathrm{yr}^{-1}} \right) \left(\frac{N}{10\,\mathrm{pc}^{-3}} \right)$$

$$\times \left(\frac{\Delta z}{1\,\mathrm{kpc}} \right)^3 \left(\frac{\tan \alpha}{\tan 1°} \right)^2 \left(\frac{R_{j,0}}{1\,\mathrm{pc}} \right)^{-2} \frac{1}{c}\,\mathrm{g\,cm}^{-3}, \tag{15}$$

where we have separated Q as the multiplication of the mean stellar wind mass-loss $\dot{M}$ times the stellar density N (for $Q = 2 \times 10^{23}\,\mathrm{g\,yr}^{-1}\,\mathrm{pc}^{-3}$, $\alpha = \tan^{-1}(R_j/\Delta z)$ is the jet half-opening angle (where we assume that $R_{j,0} \ll R_j$), and we consistently use $v_0 \simeq c$.

If we apply this formula to the simulated models, setting all fractions to one except for $Q = \dot{M}N$, we find that the minimum $\rho_0 \gamma_0$ is $\simeq 10^{-26}\,\mathrm{g\,cm}^{-3}$ for models O, while it is $\simeq 10^{-24}\,\mathrm{g\,cm}^{-3}$ for models R, with models Q between them. The relation is thus able to predict that mass load will be relevant in J4 jets and critical in J8 jets (see Figs 4, 8, A4, and A8), which have values of $\rho_0 \gamma_0 \sim 10^{-27}$ and $\sim 10^{-31}\,\mathrm{g\,cm}^{-3}$, respectively.

Although this relation does not include the effects of magnetic tension, dissipation of kinetic energy, the sudden increase of the jet opening angle once mass loading starts to be relevant, or the drop in stellar density with distance, it represents a good a priori estimate of the expected role that stellar mass load can play on jet dynamics for given initial conditions.

We can also calculate the distance at which the entrained mass equals the initial jet mass flux (note that this would imply the effective deceleration of the jet only if the momentum and energy fluxes are dominated by particles). Comparing the two terms on the right-hand
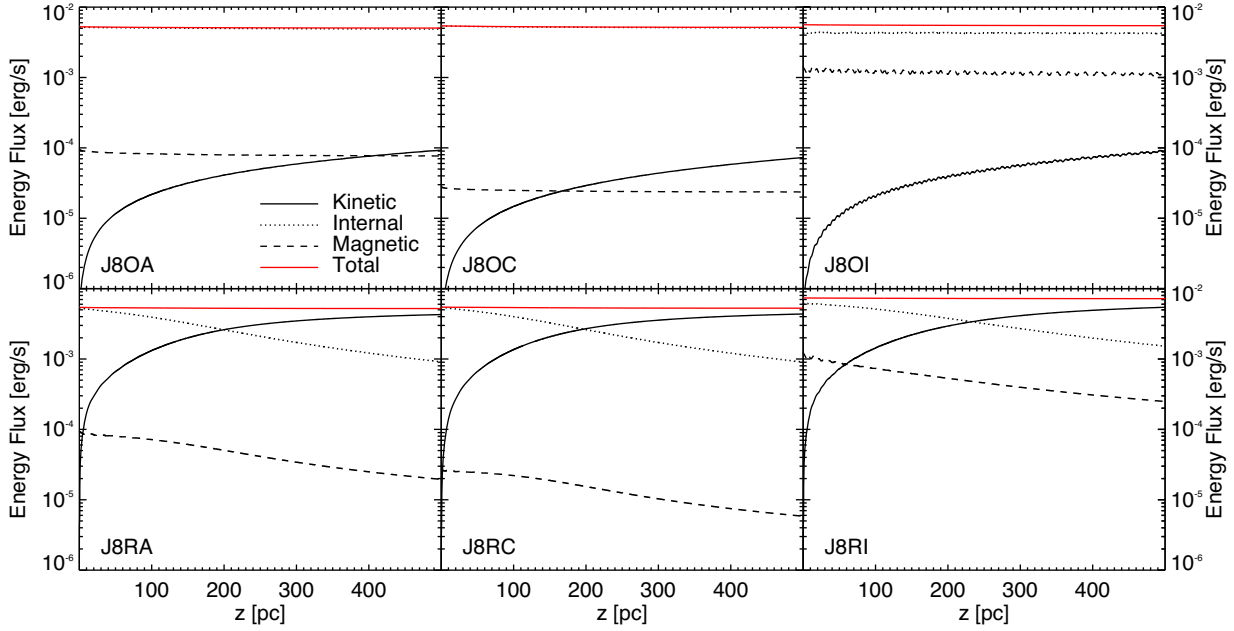
Figure 15. Energy fluxes for models J8OA (top left), J8OC (top centre), J8OI (top right), J8RA (bottom left), J8RC (bottom centre), and J8RI (bottom right) i.e. J8 models with Lorentz factors 10 (left and right) and 6 (centre), pitch angles of 45° (left and centre) and 75° (right), and with moderate (top) and heavy (bottom) mass load. The red line stands for the total flux, the dotted line for the internal energy flux, the solid line for the kinetic energy flux, and the dashed line for the magnetic energy flux.

side of equation (14), we can state that mass load will start to be relevant in terms of mass flux after a distance $\Delta z = l_m$ such that

$$\dot{M} N l_m^3 \tan^2 \alpha_j \simeq \rho_0 \gamma_0 R_{j,0}^2 c. \tag{16}$$

Now, writing the initial mass flux in terms of the jet power (assuming $v_0 \simeq c$):

$$\rho_0 \gamma_0 \pi R_{j,0}^2 c \simeq \frac{L_j}{\gamma_0 h_0}, \tag{17}$$

and taking into account that the specific enthalpy is $h_0 \geq c^2$, substitution in equation (16) allows us to get an upper bound on l_m (cf. Perucho et al. 2014),

$$l_m \leq 390 \left(\frac{1}{\gamma_0 (\tan(\alpha))^2} \right)^{1/3} \left(\frac{L_j}{10^{43} \text{ erg s}^{-1}} \right)^{1/3}$$

$$\times \left(\frac{\dot{M}}{10^{-11} \text{ M}_\odot \text{ yr}^{-1}} \right)^{-1/3} \left(\frac{N}{0.1 \text{ pc}^{-3}} \right)^{-1/3} \text{ pc.} \tag{18}$$

Although this expression is not very sensitive to variations in the parameters within an order of magnitude, it can vary with the jet opening angle, α. For an opening angle of 1°, $l_m \simeq 8.4/\gamma_0$ kpc, whereas $\alpha = 1.5°$ brings l_m to $\simeq 1$ kpc. In the case of a jet in free expansion, $\alpha \simeq 1/\gamma_0$, so if $\gamma_0 \simeq 10$, then $l_m \leq 200$ pc. Again, equation (18) does not take into account the drop in N with distance, but a large drop is not expected within the inner hundreds of parsecs for the 'core' ellipticals typically hosting FRI jets, which have roughly constant stellar densities on these scales (de Ruiter et al. 2005; Lauer et al. 2007).

4.4 Summary of jet dynamics

Fig. 16 shows a flow diagram that summarizes the different evolutionary paths discussed in this paper for mass-loaded jets. The diagram applies to both FR I and FR II relativistic jets and takes into account

the effects of the magnetic field in the evolution. In this context, we identify FR I jets as those that expand with large opening angles and decelerate to subrelativistic speeds ($\gamma \approx 1$) whereas FR II jets remain significantly relativistic and well collimated.

A drop in the ambient pressure p_a (or, equivalently, an initial jet overpressure) $[p_a/p_j\downarrow$ in the diagram] induces the expansion of the jet, which translates into an increase of the jet cross-section $[R_j\uparrow]$. The subsequent evolution depends on whether or not the jet is significantly mass loaded $[Q > Q_c ?]$.

From equation (14) it is easy to show that

$$\frac{\rho}{\rho_0} = \frac{Q \bar{R}_j^2 \Delta z}{R_j^2 \gamma v \rho_0} + \frac{R_{j,0}^2 \gamma_0 c}{R_j^2 \gamma v}, \tag{19}$$

where $\bar{R}_j$ stands for the mean value of the radius along Δz (if $R_{j,0} \ll R_j$, then $\bar{R}_j \approx R_j/2$). Thus, the comparison of the two terms on the right-hand side of the equation will determine the ratio ρ/ρ_0, namely, whether the rest-mass density of the jet decays along Δz as a result of the increase in radius, or grows as a result of the mass load. The comparison between these terms leads to the definition of a critical mass load:

$$Q_c = \frac{R_{j,0}^2}{\bar{R}_j^2} \frac{\rho_0 \gamma_0 c}{\Delta z}. \tag{20}$$

If the mass load is above this critical value [left sector of the diagram], the jet rest-mass density rises with distance $[\rho\uparrow]$, and the jet is decelerated $[\gamma\downarrow]$. This is what we clearly observe in models with higher values of Q_0 (most of the Q models and all the R ones). These jets can lead to FR Is once they have been sufficiently decelerated [top left corner of the diagram].

On the contrary, if $Q \ll Q_c$ [central/right sector of the diagram], the jet follows a well-known adiabatic expansion process in which density and pressure drop $[\rho\downarrow]$, and the Bernoulli effect takes place as long as there is internal energy available (i.e. the jet enthalpy, h, is larger than c^2 $[h = c^2 ?]$), producing acceleration $[\gamma\uparrow]$. This is seen
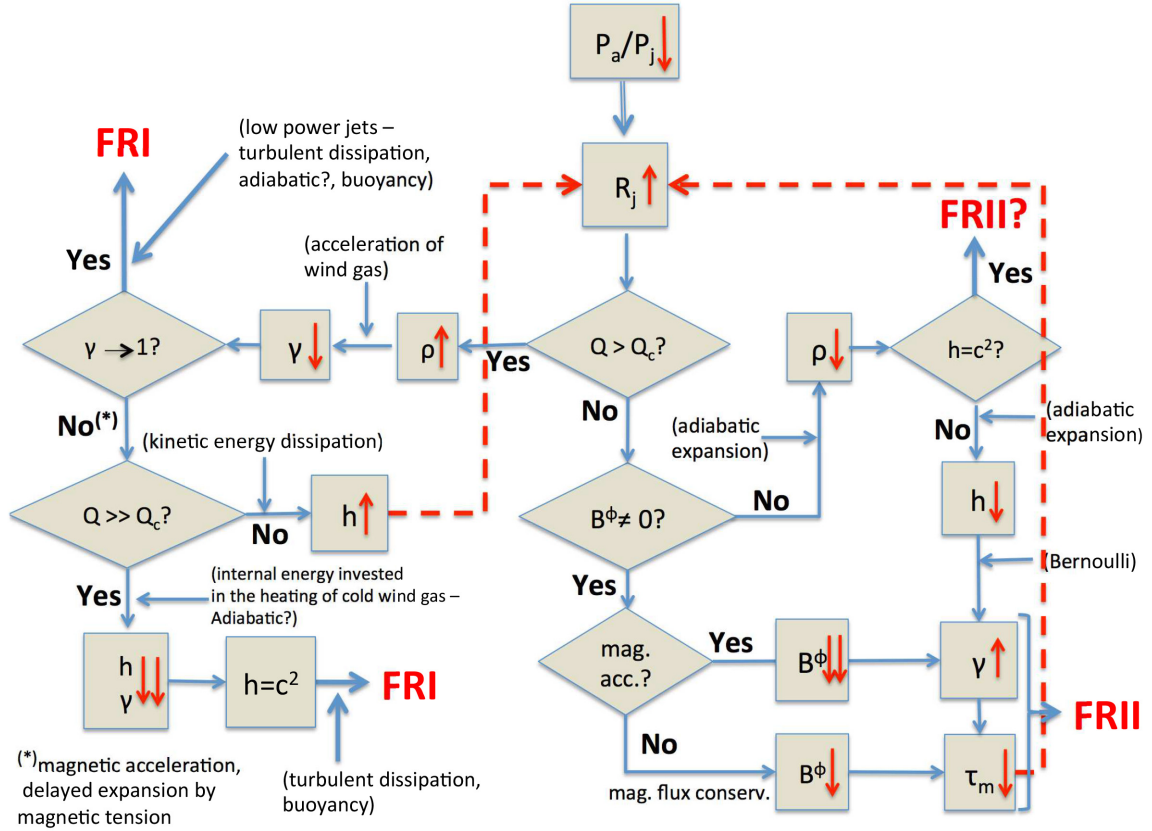
Figure 16. Flow diagram of jet evolution. The rhombi indicate options for the evolution of the flow that depend on the local jet properties, whereas the squares indicate natural consequences of the described processes. (∗) Although it has also been indicated in the diagram, it is relevant to stress that the presence of a toroidal field would slow down the processes described along the left branch, by delaying jet expansion (thus reducing the entrainment of starts and/or extending thermal acceleration) or via magnetic acceleration (see the text).

in J4O and J5O models, although the effects of mass load are also noticeable in these cases because the mass load is not very much smaller than Q_c (see Section 4.3). Jets without significant mass load (and in the absence of other disrupting instabilities, e.g. magnetic instabilities) can keep extracting internal energy and accelerating by the Bernoulli process, and remain collimated to end up as an FR II [top right corner of the diagram].

Using the energy conservation equation,

$$\pi R_{j,0}^2 \rho_0 h_0 \gamma_0^2 c = \pi R_j^2 \rho h \gamma^2 v, \tag{21}$$

leads to the following ratio for the jet enthalpy at injection and at some point downstream of the flow:

$$\frac{h_0}{h} = \frac{\rho \, R_j^2 \, \gamma^2 v}{\rho_0 \, R_{j,0}^2 \, \gamma_0^2 c}, \tag{22}$$

which, considering equations (19) and (20), can be rewritten as

$$\frac{h_0}{h} = \frac{\gamma}{\gamma_0} \left(1 + \frac{Q}{Q_c} \right), \tag{23}$$

where the term in parentheses is always larger than 1. The equation reduces to Bernoulli if $Q \ll Q_c$. In this case, the jet accelerates at the cost of reducing the specific internal energy. However, if the mass loading is large [left sector of the diagram], the internal energy can be replenished [$h\uparrow$] due to the dissipation of kinetic energy at the entrainment sites. This possibility dominates and is observed in denser, colder, and faster jets (e.g. see the upper left panels in Figs 5, 6, A3, and A6). The increase of the internal energy implies

an increase of pressure that also favours further expansion [left red broken line]. In cases in which mass load is relatively important (models Q and R), expansion has a runaway effect caused by the entrainment of more stars (or clouds) as the jet cross-section grows. As a consequence, in jets that are initially hot and with $Q \geq Q_c$, the mass entrainment increases as the jet expands [$Q \gg Q_c$] and decelerates, while the internal energy of the jet is invested in heating the entrained material [$h, \gamma \downarrow\downarrow$]. This kind of situation can lead also to FR I jets [bottom left corner of the diagram]. The self-sustained process of expansion/mass entrainment can be delayed by a toroidal field, which slows down jet expansion through the magnetic tension ($\tau_m = (B^\phi)^2/\gamma^2 R_j$), and flow deceleration if magnetic acceleration takes place (see Section 4.2).

If the jets are weakly magnetized [B^ϕ?]; bottom right sector of the diagram, super-Alfvénic flows would overexpand beyond pressure equilibrium with the ambient medium, triggering recollimation shocks; or would continue expanding to longer distances, if the pressure gradient is shallow. In many of our simulations, we see that non-magnetized jets (models N, represented by blue lines in the line plots) show larger opening angles than magnetized jets. If the jets are strongly magnetized, they can undergo magnetic acceleration if differential expansion is induced (see e.g. Komissarov 2012, and references therein) and generate a fast drop in the toroidal field [$B^\phi \downarrow\downarrow$] and a consequent relative increase in the Lorentz factor. The expansion also leads to a drop in the field, albeit slower [$B^\phi \downarrow$], due to conservation of the magnetic flux. In both cases, there is a relative drop of the magnetic tension [$\tau_m \downarrow$], which may allow further

expansion [right red broken line].[6] We can see that the situations depicted in the right sector of the diagram end up in jet acceleration, thus typically producing large-scale FR II morphologies.

It is relevant to stress that in this flow diagram, we describe competing effects that can take place at the same time for a given jet and can either have opposite effects, or contribute in the same direction.

4.5 Astrophysical implications

In Laing & Bridle (2014), the authors modelled a number of FR I jets by fitting distributions of velocity, rest-frame emissivity, and magnetic field ordering to the brightness and polarization distributions of the sources. A series of common (or frequent) features were found:

(i) an initial brightness and geometrical flaring beyond the dense galactic corona,

(ii) development of a wide velocity distribution and deceleration (from $v \simeq 0.8\,c$ to $v \leq 0.4\,c$ on axis),

(iii) a region of high emissivity roughly coincident with the deceleration,

(iv) recollimation to a conical expansion with roughly constant velocity farther downstream,

(v) a transformation of the magnetic field structure from a mixture of an ordered toroidal component and a disordered longitudinal one (with the longitudinal field dominating) at the jet base to mainly toroidal after deceleration.

The models of emissivity and field-component ratio are not consistent with adiabatic losses and flux freezing alone. The authors conclude that ongoing particle acceleration is required, consistent with the short cooling times for observed X-ray synchrotron emission.

The brightness flaring starts at distances that range from 0.7 to 2 kpc, approximately, whereas the range of distances at which strong deceleration starts is more spread, although it happens within the inner 4 kpc for most of the sources. The position of the brightness flaring sets the distance from which the model fitted to the sources in Laing & Bridle (2014) can give reasonable determinations of the physical parameters. This is, thus, beyond the region that we have covered in this work (we also note that our approximation does not allow us to run simulations with $v_j \simeq 0.8\,c$, which is the typical fitted velocity at that distance in Laing & Bridle 2014).

The simulations that we show here would cover the inner region, in which the modelling of FR I jets by Laing & Bridle is much less reliable due to the narrowness and faintness of both the jets and the counter-jets. Our results describe the jet structure in the region of the dense corona, close to the active nucleus. In this region, FR I jets are probably still relativistic, as revealed by the brightness asymmetries in VLBI images of those FR I jets that can be imaged (see e.g. the strong brightness asymmetry in the case of NGC 315; Lister et al. 2018). Therefore, the approximation of jet axial speed close to c that is required by our simulations remains valid.

Our simulations show that jets with powers $L_j \simeq 10^{43}\,\mathrm{erg\,s^{-1}}$ can be decelerated from velocities that are close to c to that given by the models at the onset of the flaring region, $\simeq 0.8\,c$ for sufficient mass-loss rates per star and stellar densities within the galactic core. These are nevertheless possibly too large with respect to the expected ones from typical stellar populations in these galaxies. In Figs 17 and 18, we show the evolution of rest-mass density and Lorentz

---

[6]We actually observe hints of magnetic acceleration in those jets with non-conical expansion (see Figs 14, 15, 3, and A9, and Section 4.2).
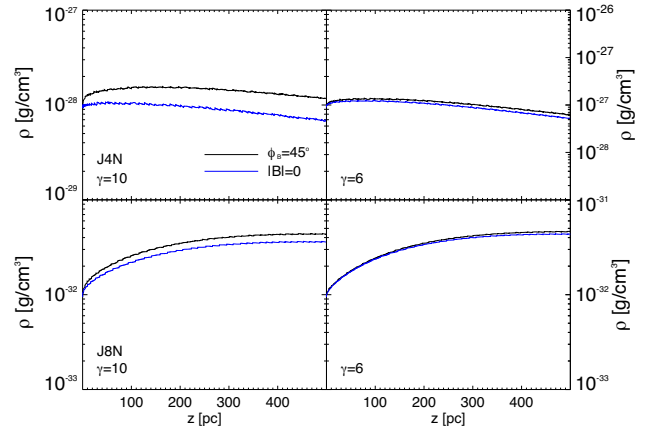
Figure 17. Rest-mass density versus distance for models J4N$_-$ (top panels) and J8N$_-$ (bottom panels) with Lorentz factor 10 (left column), and 6 (right column). In each plot, the black and blue lines represent the jets with mean pitch angles $\phi_B = 45°$, and purely hydro models, respectively.
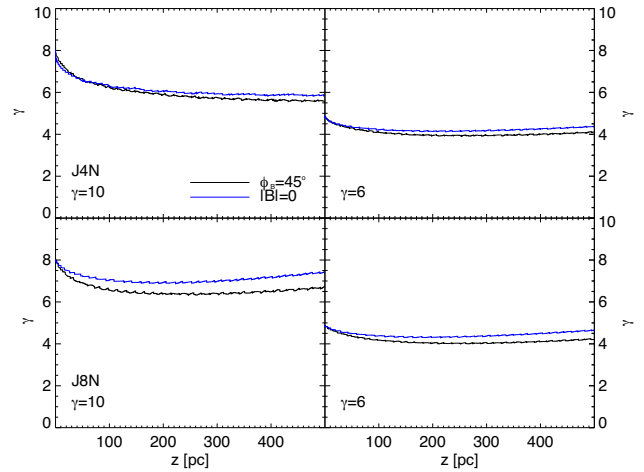
Figure 18. Mean jet Lorentz factor versus distance for models J4N$_-$ (top panels) and J8N$_-$ (bottom panels) with Lorentz factor 10 (left column), and 6 (right column). In each plot, the black and blue lines represent the jets with mean pitch angles $\phi_B = 45°$, and purely hydro models, respectively.

factor obtained for a number of J4N and J8N models, i.e. those with the expected mass load in elliptical galaxies (see Table 3). The results (also for the radius and the jet temperature, not shown) are qualitatively very similar to the equivalent J4O and J8O models and confirm that, although it can have a non-negligible effect on the jet parameters (mild deceleration and an increase in the rest-mass density are observed), stellar mass load cannot, by itself, explain jet deceleration to mildly relativistic or subrelativistic speeds as it happens in classical FR I jets (as anticipated by Laing & Bridle 2002b; Perucho et al. 2014).

In Section 4.3, we have shown that even well-collimated jets can mass load in quantities equivalent to their initial mass fluxes at distances that are of the order of the flaring distances given in Laing & Bridle (2014). Whether this load is also sufficient to trigger the emissivity flaring via the shocks and turbulence triggered by the jet–star interactions (e.g. Bosch-Ramon et al. 2012; Perucho et al. 2017) remains to be studied. However, the visible drop in the jet Lorentz factor and the increase (or delayed decrease) in the jet rest-mass density or temperature (not shown) produced by this process

even for the expected stellar populations in ellipticals (see Figs 17 and 18), shows that it can efficiently contribute to the dissipation of the jet energy flux and to its radiative output at these scales (e.g. Wykes et al. 2015; Vieyro et al. 2017).

Furthermore, our simulations also show that, when mass load becomes sufficient, the jets undergo an expansion that resembles the geometrical flaring observed in FR I jets, even in slowly decaying ambient pressures (see Figs 3 and A9). This effect would be exaggerated in the case of rapidly decreasing atmospheres outside the dense galactic cores, which is where it takes place in the observed FR I sources, according to Laing & Bridle (2014). It is important to stress that once the jet inner spine is decelerated, the entrainment triggered at the boundaries, probably by small-scale instabilities (e.g. Meliani & Keppens 2007, 2009; Matsumoto & Masada 2013; Matsumoto, Aloy & Perucho 2017; Toma, Komissarov & Porth 2017; Gourgouliatos & Komissarov 2018a, b) can reach the axis in shorter distances than in the case of jets with large Lorentz factors.

Finally, adding the effect of mass load by stars to the possible role of stars in triggering mixing with the ambient medium, as suggested in Perucho (2020), could well be a sufficient combination of processes to explain jet deceleration in relatively powerful FR I sources, whereas stellar mass-loss could be a sufficient mechanism for jet deceleration in less powerful jets (Perucho et al. 2014).

5 CONCLUSIONS

We have run RMHD simulations of stationary jets, with a source term in the mass equation that accounts for mass loading by stellar winds within the host galaxy. We have simulated jets with a total power of 10^{43} erg s^{-1} but with a wide range of internal energies and densities, and different magnetic field configurations, Lorentz factors, and mean stellar populations (i.e. mean stellar wind mass-loss). The models are injected in transversal equilibrium, which is updated for each spatial step along the jet axis, as the injected particles and the ambient medium pressure change the jet-to-environment conditions.

Our results show that:

(i) Jets with 10^{43} erg s^{-1} may undergo mild deceleration even for old stellar populations, which, in the frame of the suggestion that stars may also trigger jet–ISM mixing at the jet boundary (Perucho 2020), can altogether represent an efficient deceleration mechanism for classical FR I jets.

(ii) Initially, dilute and hot models cool and mass load very rapidly, changing from an electron–positron dominated jet to an electron–proton dominated jet.

(iii) Initially, denser and faster jets can undergo heating caused by the dissipation of kinetic energy as they are mass loaded.

(iv) The toroidal field acts to collimate the flow, with a double effect with respect to non-magnetized jets:

   (i) Bernoulli acceleration becomes more gradual, and
   (ii) it prevents the entrainment of further stars by preventing fast jet expansion.

(v) The effects of entrainment are that:

   (i) the magnetic field structure tends to be dominated by the toroidal field, by forcing jet expansion, and
   (ii) the ratio of magnetic energy to internal energy densities drops with distance.

(vi) A population of stars dominated by red giants would rapidly decelerate the jets to mildly relativistic speeds. However, such a population is not present in typical FR I host galaxies, so it is improbable that stellar winds alone can decelerate the jets.

(vii) In the case of strong mass load, we have observed a correlation between differential expansion and a drop in magnetic energy flux that delays deceleration, i.e. that is invested into flow acceleration.

(viii) The mass load by stars in the dense corona of galaxies, where the stellar density is larger, could trigger the initial jet deceleration before the brightness and geometrical flaring start.

(ix) In general, mass load might contribute to the change of the jet properties and composition (loading protons) along its spatial evolution and can efficiently generate dissipation of the jet energy flux and cause part of the observed radiative output at these scales.

Future simulations should include a full three-dimensional, dynamic approach to the problem, introducing cooling terms to account for the possible non-adiabatic behaviour of jet evolution during deceleration (Laing & Bridle 2014). In addition, simulations of jet evolution under the constant perturbation of star crossings at the boundaries, as suggested by Perucho (2020), should be performed, although the different scales that this scenario implies strongly complicate the set-ups.

DATA AVAILABILITY

The data underlying this article will be shared on reasonable request to the corresponding author.

REFERENCES

Aharonian F. A., Barkov M. V., Khangulyan D., 2017, ApJ, 841, 61
Araudo A. T., Bosch-Ramon V., Romero G., 2013, MNRAS, 436, 3626
Baczko A.-K. et al., 2016, A&A, 593, A47
Barkov M. V., Aharonian F. A., Bosch-Ramon V., 2010, ApJ, 724, 1517
Barkov M. V., Aharonian F. A., Bogovalov S. V., Kelner S. R., Khangulyan D., 2012, ApJ, 749, 119
Bednarek W., Protheroe R. J., 1997, MNRAS, 287, L9
Begelman M. C., Blandford R. D., Rees M. J., 1984, Rev. Mod. Phys., 56, 2
Bicknell G. V., 1984, ApJ, 286, 68
Bicknell G. V., 1994, ApJ, 422, 542
Bosch-Ramon V., Perucho M., Barkov M. V., 2012, A&A, 539, A69
Bowman M., Leahy J. P., Komissarov S. S., 1996, MNRAS, 279, 899
Carilli C. L., Barthel P. D., 1996, A&AR, 7, 1
Celotti A., Ghisellini G., 2008, MNRAS, 385, 283
Choi E., Wiita P. J., 2010, ApJS, 191, 113
de Ruiter H. R., Parma P., Capetti A., Fanti R., Morganti R., Santantonio L., 2005, A&A, 439, 487
De Young D. S., 1986, ApJ, 307, 62
De Young D. S., 1993, ApJ, 405, L13
Fanaroff B. L., Riley J. M., 1974, MNRAS, 167, 31
Fuentes A., Gómez J. L., Martí J. M., Perucho M., 2018, ApJ, 860, 121
Giovannini G., Cotton W. D., Feretti L., Lara L., Venturi T., 2001, ApJ, 552, 508
Gourgouliatos K. N., Komissarov S. S., 2018a, Nat. Astron., 2, 167
Gourgouliatos K. N., Komissarov S. S., 2018b, MNRAS, 475, 125
Hubbard A., Blackman E. G., 2006, MNRAS, 371, 1717
Komissarov S. S., 1994, MNRAS, 269, 394

Komissarov S. S., 2012, in Boettcher M., Harris D. E., Krawczynski H., eds, Relativistic Jets from Active Galactic Nuclei. Wiley, Berlin, p. 81

Komissarov S. S., Porth O., Lyutikov M., 2015, ComAC, 2, 9

Laing R. A., 1993, in Burgarella D., Livio M., O'Dea C. P., eds, Space Telescope Science Institute Symposium Series, Astrophysical Jets. Cambridge Univ. Press, Cambridge, p. 95

Laing R. A., 1996, in Hardee P. E., Bridle A. H., Zensus J. A., eds, Proc. IAU Symp. 175, Energy Transport in Radio Galaxies and Quasars. Kluwer, Dordrecht, p. 147

Laing R. A., Bridle A. H., 2002a, MNRAS, 336, 328

Laing R. A., Bridle A. H., 2002b, MNRAS, 336, 1161

Laing R. A., Bridle A. H., 2014, MNRAS, 437, 3405

Lauer T. R. et al., 2007, ApJ, 664, 226

Lister M. L., Aller M. F., Aller H. D., Hodge M. A., Homan D. C., Kovalev Y. Y., Pushkarev A. B., Savolainen T., 2018, ApJS, 234, 12

Martí J. M., 2015, MNRAS, 452, 3106

Martí J. M., Perucho M., Gómez J. L., 2016, ApJ, 831, 163

Matsumoto J., Masada Y., 2013, ApJ, 772, L1

Matsumoto J., Aloy M. A., Perucho M., 2017, ApJ, 472, 1421

Meliani Z., Keppens R., 2007, A&A, 475, 785

Meliani Z., Keppens R., 2009, ApJ, 705, 1594

Meyer E. T., Fossati G., Georganopoulos M., Lister M. L., 2011, ApJ, 740, 98

Müller C. et al., 2014, A&A, 569, A115

Murase K., Oikonomou F., Petropoulou M., 2018, ApJ, 865, 124

Perucho M., 2020, MNRAS, 494, L22

Perucho M., Martí J. M., 2007, MNRAS, 382, 526

Perucho M., Martí J. M., Laing R. A., Hardee P. E., 2014, MNRAS, 441, 1488

Perucho M., Bosch-Ramon V., Barkov M. V., 2017, A&A, 606, A40

Phinney E. S., 1983, PhD thesis, Univ. Cambridge

Rossi P., Mignone A., Bodo G., Massaglia S., Ferrari A., 2008, A&A, 488, 795

Synge J. L., 1957, The Relativistic Gas. North-Holland Publishing Company, Amsterdam

Toma K., Komissarov S. S., Porth O., 2017, MNRAS, 472, 1253

Torres-Albà N., 2020, Nat. Astron., 4, 448

Torres-Albà N., Bosch-Ramon V., 2019, A&A, 623, A91

Vieyro F. L., Torres-Albà N., Bosch-Ramon V., 2017, A&A, 604, A57

Walker R. C., Hardee P. E., Davies F. B., Ly Ch., Junor W., 2018, ApJ, 855, 128

Wang Y., Kaiser C. R., Laing R., Alexander P., Pavlovski G., Knigge C., 2009, MNRAS, 397, 1113

Worrall D. M., Birkinshaw M., Laing R. A., Cotton W. D., Bridle A. H., 2007, MNRAS, 380, 2

Wykes S. et al., 2013, A&A, 558, A19

Wykes S., Hardcastle M. J., Karakas A. I., Vink J. S., 2015, MNRAS, 447, 1001

Zamaninasab M., Clausen-Brown E., Savolainen T., Tchekhovskoy A., 2014, 510, 126

SUPPORTING INFORMATION

Supplementary data are available at *MNRAS* online.

Appendix A. Supplementary Material.

Please note: Oxford University Press is not responsible for the content or functionality of any supporting materials supplied by the authors. Any queries (other than missing material) should be directed to the corresponding author for the article.

This paper has been typeset from a TEX/LATEX file prepared by the author.